REVIEW ARTICLE
https://doi.org/10.1038/s41565-021-00936-x

nature nanotechnology

Van der Waals heterostructures for spintronics and opto-spintronics

Juan F. Sierra[1]✉, Jaroslav Fabian[2], Roland K. Kawakami[3], Stephan Roche[1,4] and Sergio O. Valenzuela[1,4]✉

The large variety of 2D materials and their co-integration in van der Waals heterostructures enable innovative device engineering. In addition, their atomically thin nature promotes the design of artificial materials by proximity effects that originate from short-range interactions. Such a designer approach is particularly compelling for spintronics, which typically harnesses functionalities from thin layers of magnetic and non-magnetic materials and the interfaces between them. Here we provide an overview of recent progress in 2D spintronics and opto-spintronics using van der Waals heterostructures. After an introduction to the forefront of spin transport research, we highlight the unique spin-related phenomena arising from spin–orbit and magnetic proximity effects. We further describe the ability to create multifunctional hybrid heterostructures based on van der Waals materials, combining spin, valley and excitonic degrees of freedom. We end with an outlook on perspectives and challenges for the design and production of ultracompact all-2D spin devices and their potential applications in conventional and quantum technologies.

In the past few years, van der Waals (vdW) heterostructures[1,2] comprising a variety of 2D layered materials have emerged as potential building blocks for future ultrafast and low-power electronic and spintronic devices. Graphene is an ideal spin channel owing to its spin diffusion length that reaches several micrometres at room temperature, gate-tunable carrier concentration and extremely high carrier mobility[3–5]. Semiconducting transition metal dichalcogenides (TMDCs)[6] such as MX_2 (M = W, Mo; X = S, Se, Te) and topological insulators (TIs) such as Bi_2Te_3 possess strong spin–orbit coupling (SOC), which allows for the electrical generation and manipulation of spins. Semiconducting TMDCs further possess a strong spin–photon coupling that enables optical spin injection, while 2D magnets[7] bring capabilities for spin filtering and non-volatile data storage.

Novel functionalities arise due to the atomically thin nature of 2D materials, which facilitates much stronger electrostatic gating effects than with conventional materials to achieve, for instance, voltage-controlled magnetism. Furthermore, the integration of graphene, TMDCs, TIs and 2D magnets into vdW heterostructures not only combines the respective material functionalities but also imprints properties through proximity interactions across interfaces[8], enabling the design of artificial structures with unique characteristics. Such properties provide opportunities[9,10] for memory applications, spin interconnects, spin-transistors, microwave nano-oscillators, low-power reconfigurable logic, and flexible or wearable spintronic platforms[11,12] (Box 1).

This Review presents the state of the art and future prospects for vdW heterostructures in spintronics and opto-spintronics, with a special focus on magnetic and spin–orbit proximity effects and the emerging phenomena deriving from them. Covering recent experimental and theoretical developments, the Review is divided in four main sections. The first section briefly surveys recent progress in spin injection and detection, including the integration of opto-electronic elements, and then outlines the contemporary understanding of spin dynamics in 2D materials. This description is complemented by an overview of materials that can be used to enhance the spin properties or further create multifunctional 2D spintronic devices (Box 1). The second section focuses on proximity-induced SOC, which is central in modern spintronics as it can enhance the magnetic properties of 2D magnets as well as provide spin filtering, spin manipulation and efficient charge-to-spin interconversion (CSI) functionalities. The third section addresses magnetic proximity effects, which can be harnessed in memory elements, reconfigurable spin-logic circuits and novel spin-valleytronics applications. Besides the vast catalogue of material combinations, vdW heterostructures establish new concepts based on twist angle and stacking control between crystallographic lattices that can strongly dictate the nature and strength of proximity phenomena. Finally, the fourth section discusses potential applications and future research directions and perspectives.

Spin dynamics in 2D materials

Recent advances in spin injection and detection. Spin dynamics is typically investigated using lateral devices in a non-local electrical configuration[3,5] or, alternatively, using spectroscopic methods in optically active materials[13]. Lateral spin devices rely on efficient spin injection and detection, with tunnel barriers playing a crucial role in alleviating the conductance mismatch problem[14], which limits the effective spin polarization P_s of the injector and detector contacts (Fig. 1a). Early studies with graphene as a spin channel used MgO, Al_2O_3, TiO_2 and amorphous carbon barriers[15–17] but the emergence of alternative insulators could improve various aspects of device performance. SrO barriers, grown by the evaporation of Sr in the presence of molecular oxygen, lead to robust operation with high bias (~2 V) to achieve large spin accumulation[18]. Barriers composed of 2D materials produce high P_s. Fluorinated graphene, obtained by exposure to XeF_2 gas, yields $P_s > 40\%$ (ref. [19]), whereas hexagonal boron nitride (hBN), using stacking and transfer

[1]Catalan Institute of Nanoscience and Nanotechnology (ICN2), CSIC and The Barcelona Institute of Science and Technology (BIST), Barcelona, Spain. [2]Institute for Theoretical Physics, University of Regensburg, Regensburg, Germany. [3]Department of Physics, Ohio State University, Columbus, OH, USA. [4]Institució Catalana de Recerca i Estudis Avançats (ICREA), Barcelona, Spain. ✉e-mail: juan.sierra@icn2.cat; SOV@icrea.cat

Box 1 | Designer vdW heterostructures for (opto)spintronics: material functionalities

Key practical elements in spintronics are the injection, transport or communication, manipulation and detection of spin information[10,13,176,177]. Each of these aspects, represented in the figure, can benefit from the unique properties of 2D materials. While spin communication requires low spin–orbit materials, spin injection, detection and manipulation can be achieved by creating multifunctional vdW heterostructures, which include materials with magnetic exchange interaction (MEI) and/or large SOC.

Spin communication over practical distances has already been demonstrated in graphene[31,178] and black phosphorus[22] at room temperature, enhanced by vdW encapsulation with hexagonal boron nitride (hBN)[30]. Spin logic and multiplexer devices have been proposed, using spin accumulation[53], gate dependence of spin lifetimes and/or drift currents[54,179].

Spin injection and detection use several approaches[10,176]. They involve insulating 2D ferromagnets, metallic 2D ferromagnets in combination with insulating tunnel barriers, or topological insulators (TIs) and other large-SOC materials through CSI mechanisms, such as the spin Hall effects (SHE) and spin galvanic effects (SGE).

Optical spin injection in graphene, using TMDCs[27], has also been demonstrated[28,29]. Magnetic tunnel junctions, combining 2D ferromagnets and insulating hBN barriers, or tunnel filters comprising insulating (anti)ferromagnetic materials, could be used in ultracompact low-power memory elements[10,176].

Spin manipulation and control, as well as spin injection and detection, can be engineered via proximity-induced SOC and proximity-induced MEI by adjacent (insulating) large-SOC materials (for example, TMDCs and TIs) and (anti)ferromagnets, respectively. Magnetization switching and precession in memory elements could be achieved with spin–orbit torques (SOTs)[10] using CSI in materials with large SOC, either of intrinsic origin or acquired by proximity effects. Novel spin-transistor configurations and spin polarizers, which take advantage of proximitized spin–valley coupling in graphene, have been experimentally demonstrated[87,89,90]. The atomically thin nature of 2D (anti) ferromagnets further enables the manipulation of their magnetic state using electric fields[157], whereas twist-angle and stacking control between crystallographic lattices add yet other versatile knobs to engineer the nature and strength of proximity effects. In the figure, V_{G1-4} denote local gates, ω_1 is the frequency of the incident light, **M** the magnetization vector of the ferromagnet and **T** the exerted torques.

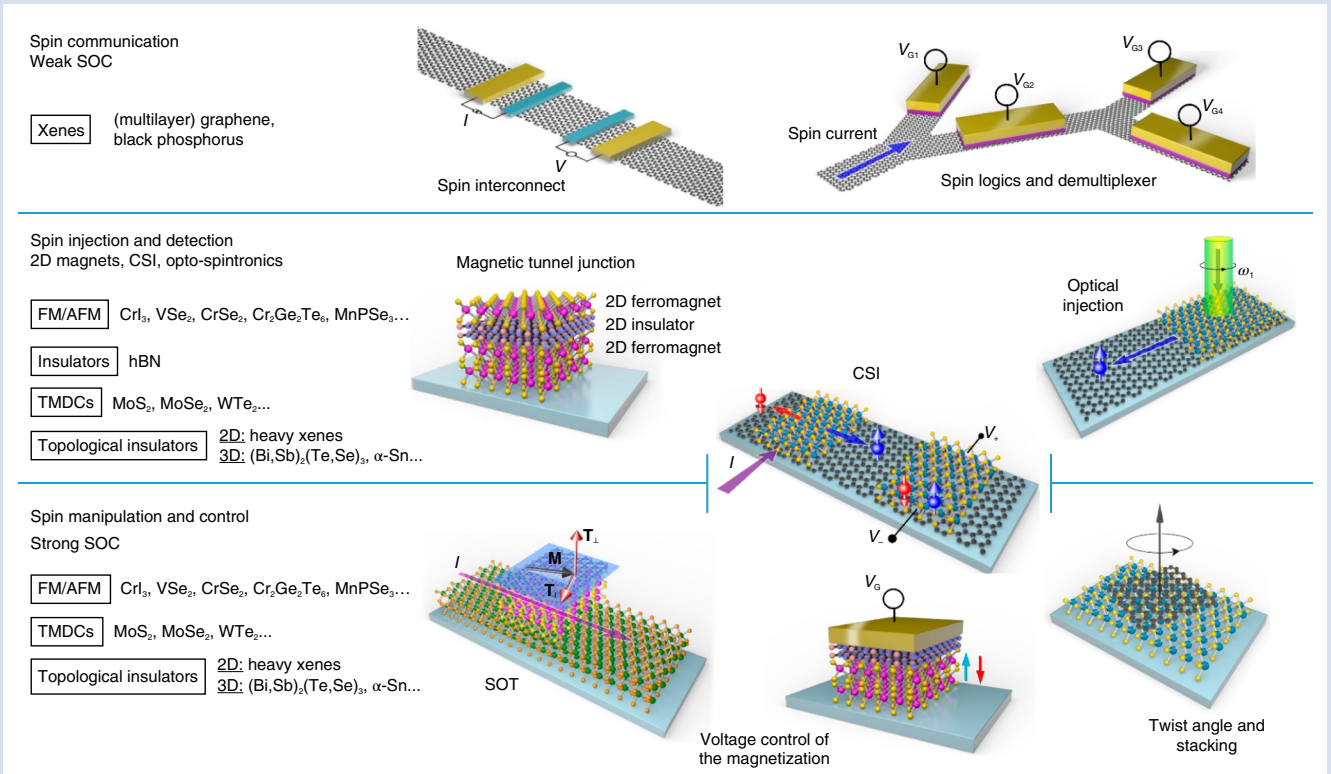

methods, efficiently injects spins into graphene[20,21] and black phosphorus[22]. With graphene, hBN-based injectors display a differential spin polarization that varies with applied voltage bias, reaching absolute values above 100% and even changing sign[21]. Beyond planar contacts, 1D edge contacts have been used for spin injection into hBN-encapsulated graphene[23].

Optical selection rules together with Faraday and Kerr microscopies, broadly used in semiconducting materials[13], are valuable tools to investigate spin-valley dynamics and spin coherence in TMDCs[24–26]. Typically, a pump laser illuminates individual crystals with right- or left-circularly polarized light at specific wavelengths to target an exciton transition, generating spin-polarized electrons and holes in the K or K′ valley, respectively (Fig. 1b). The spin polarization can then be detected by means of the optical Kerr rotation of a linearly polarized laser probe.

When embedded in vdW heterostructures, TMDCs enable a new platform for opto-spintronics[27] (Box 1). As demonstrated in MoS_2– and WSe_2–graphene heterostructures, the spin-polarized

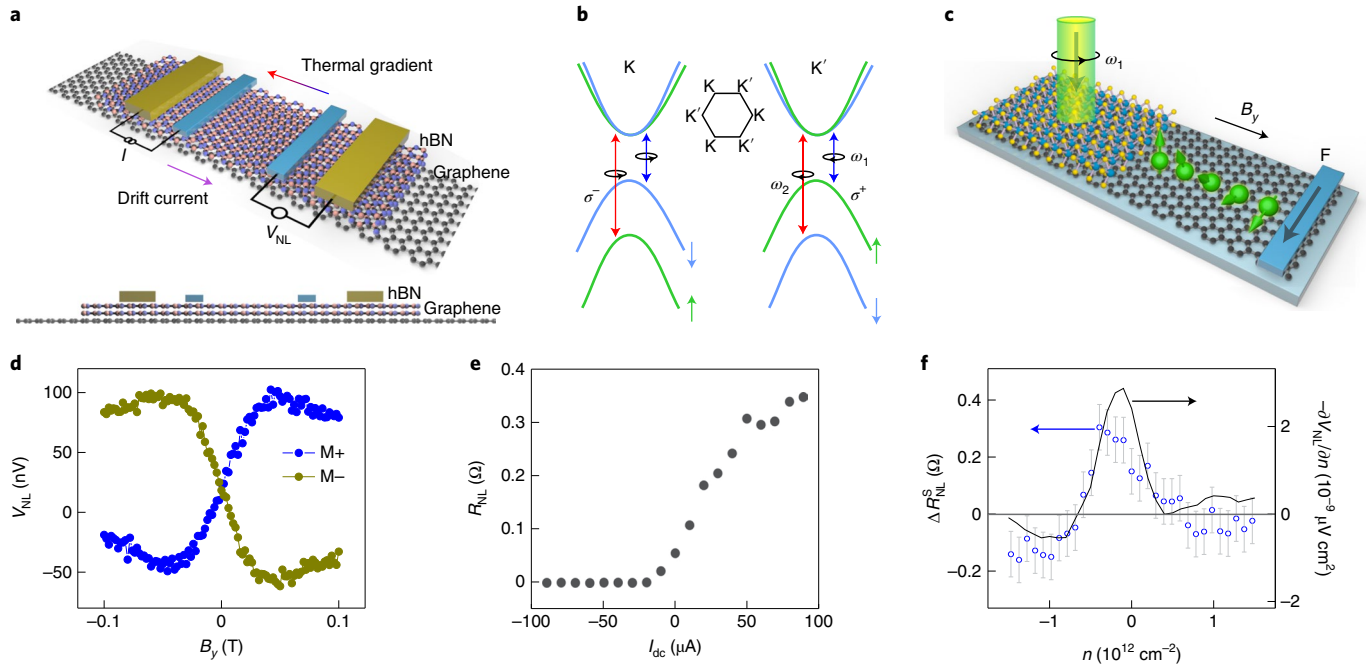

Fig. 1 | Spin injection and spin transport. a, Top: illustration of a lateral graphene–hBN spin device with current (I) and voltage (V_{NL}) leads in the non-local configuration scheme and control by electric and thermal drifts. Blue (inner) contacts are ferromagnetic, whereas yellow (outer) contacts are preferably non-magnetic. Bottom: cross-section of the device. **b**, Schematic band structure and optically excited transitions of a monolayer TMDC at the K (left) and K′ (right) valleys with left (σ^-) and right (σ^+) circularly polarized light with frequencies $\omega_{1,2}$. **c**, Optical spin injection from monolayer TMDC into graphene and subsequent lateral spin transport. The spin current is remotely detected using the spin-sensitive (ferromagnetic) contact F. The injected spins are initially oriented out-of-plane and rotate under the influence of applied magnetic field B_y as they diffuse towards F, eventually becoming aligned with its magnetization. **d**, V_{NL} measured at probe F in **c** as a function of B_y; V_{NL} exhibits an antisymmetric spin precession signal whose sign changes when the magnetization **M** of the detector F is flipped. **e**, Spin signal $R_{NL} = V_{NL}/I$ as a function of the drift current I_{dc} applied along the spin channel as shown in **a**. The modulation is driven by a change in the effective λ_s, which increases or decreases when I_{dc} flows in favour of or against the spin current, respectively. **f**, Spin signal change ΔR^S_{NL} as a function of the graphene carrier density n induced by the presence of a thermal gradient in the spin channel as shown in **a**. Figure adapted with permission from: **d**, ref. [28], American Chemical Society; **e**, ref. [55], American Chemical Society; **f**, ref. [56], Springer Nature Limited.

carriers generated in the TMDC transfer into the neighbouring graphene[28,29] (Fig. 1c). The resulting antisymmetric Hanle spin precession curve (Fig. 1d) under the influence of an applied magnetic field B_y provides unambiguous proof of the optical spin injection.

Spin dynamics and relaxation. The spin propagation is characterized by the spin relaxation length λ_s, given by $\lambda_s = \sqrt{D_s \tau_s}$ where D_s is the spin diffusion constant and τ_s is the spin lifetime. In the diffusive regime, D_s is obtained from transport measurements, whereas various possible SOC mechanisms, either intrinsic or extrinsic, introduce sources of spin relaxation and dictate the ultimate values of τ_s and λ_s (ref. [13]). At room temperature, graphene displays spin-transport figures of merit for spin communication that outperform those of all other materials (Box 1). In hBN-protected graphene, τ_s can be larger than 10 ns (with $\lambda_s \approx 30\,\mu$m)[30]. Room-temperature spin-diffusion lengths reaching 10 μm were further achieved in chemical vapour deposition (CVD)-grown graphene on silicon oxide (SiO_2) substrates[31]. Black phosphorus also transports spins efficiently; when encapsulated with hBN, $\tau_s \approx 0.7$ ns and $\lambda_s \approx 2.5\,\mu$m at room temperature[22]. In TMDCs, spin relaxation has been investigated using optical orientation and time-resolved Kerr rotation. Reported spin-valley lifetimes at low temperature (a few kelvin) exceed several nanoseconds in electron-doped CVD-grown MoS_2 and WS_2 monolayers[24,32] and are about 80 ns for holes in CVD WSe_2 monolayers[33]. Although they are significantly longer in exfoliated WSe_2 (100 ns for electrons[25] and 1 μs for holes[25,26]) all temperature-dependent studies show a fast decrease with temperature. A strikingly different behaviour has been observed in $MoSe_2$, with the longest lifetime of ~100 ns found at room temperature, albeit probably corresponding to non-itinerant carriers[34]. Efficient generation of pure and locked spin-valley diffusion current was demonstrated in exfoliated WS_2–WSe_2 heterostructures at 10 K by pump–probe spectroscopy[35]. Excitons are created in WSe_2, and the subsequent fast transfer of excited electrons to WS_2 suppresses the exciton-valley depolarization channel. The recombination of electrons in WS_2 with holes in WSe_2 leaves an excess of holes in one of the WSe_2 valleys, which are found to live for longer than 20 μs and propagate over 20 μm.

The mechanisms leading to spin relaxation in 2D materials are very rich and frequently unique to each material. This is illustrated by the case of graphene. Theoretical calculations describe a wide range of possible SOC sources, through the symmetry, spatial range and strength of spin-conserving and non-spin-conserving events. Intrinsic and Rashba contributions give rise to a small spin-splitting[36] of tens of microelectronvolts, as corroborated experimentally[37]. Early theoretical work indicated that τ_s could be in the millisecond range[3]. However, follow-up studies, introducing realistic descriptions of impurities (magnetic defects such as hydrogen adsorbents serving as spin-flip resonant scatterers[38,39]) or subtle mechanisms such as spin–pseudospin coupling[40,41], have provided alternative explanations for the observed τ_s in the nanosecond and sub-nanosecond range. These studies account for the energy dependence of τ_s, with the most universal feature being a minimum near the charge neutrality point. The underlying origin for the spin relaxation has been described using the Elliot–Yafet[42] or Dyakonov–Perel[43] mechanisms; however, these are only strictly applicable in

disordered systems with short mean free paths[44]. Some progress in analysing spin dynamics in the ballistic limit, as well as possible fingerprints in spin precession measurements, has been made[45]. In polycrystalline graphene, theoretical analysis has revealed universal spin diffusion lengths dictated by the absolute strength of the substrate-induced Rashba SOC in the Dyakonov–Perel regime[44] ($\lambda_s = \hbar v_F/2\lambda_R$, where $\hbar$ is the Planck constant, v_F the Fermi velocity and λ_R the Rashba SOC strength). Despite important progress, a full correspondence between theory and experiment is still missing. Indeed, the predominance of Rashba SOC in spin transport should manifest in a spin-transport anisotropy[44], where the out-of-plane spin lifetime $\tau_{s,\perp}$ is half the in-plane one $\tau_{s,\parallel}$. An electric field modulation of the spin relaxation anisotropy ratio $\zeta = \frac{\tau_{s,\perp}}{\tau_{s,\parallel}}$, consistent with the presence of Rashba SOC, was reported in graphene encapsulated with hBN[46]. However, it has been argued[47,48] that the application of large out-of-plane magnetic fields could affect the determination of ζ. Recent experimental studies[47–50] have failed to establish a significant spin lifetime anisotropy, suggesting that either magnetic resonant spin-flip scattering or deformation-induced gauge pseudo-magnetic fields randomize the spatial direction of the effective SOC field[38,39,47,49]. Remarkably, as discussed below, a known SOC can be made dominant in proximitized graphene and, in contrast to graphene, the spin dynamics in some situations has been predicted and is well understood[51].

Beyond graphene, progress has been modest. Spin relaxation in few-layer black phosphorus seems to follow the Elliot–Yafet mechanism, as suggested by the similar temperature dependence of the measured τ_s and the momentum lifetime[22]. In TMDCs, the long spin-valley lifetimes confirm the expectation of spin-valley locking, which manifests more strongly in the valence band. The relaxation is expected to be mediated by intravalley decoherence mechanisms, dominating electron spin lifetime; however, spin-flip processes between valleys, requiring simultaneous scattering of both valley and spin degrees of freedom, yield slow relaxation rates for holes. As temperature increases, the behaviour becomes increasingly complex, as relaxation pathways involving secondary valleys and different phonon-mediated intervalley scattering rates may play a role in determining the spin lifetimes[34].

Current and thermal spin current drift. Large λ_s may facilitate the realization of all-spin reprogrammable operations by controlling spin currents in lateral devices[3,52] (Box 1). In this regard, an XOR (exclusive OR) magnetologic gate has been experimentally demonstrated at room temperature by electrical bias tuning of the spin injection in graphene[53]. This demonstration was followed by the proposal of a gate-driven demultiplexer using local voltage gates to tune the spin currents[54]. Further experimental progress has been achieved in the control of spin currents via carrier and thermal drift effects. Lateral drift fields in bilayer graphene (BLG), caused by a charge current (Fig. 1a), were shown to modulate the spin signal at room temperature[55] (Fig. 1e). More recently, the use of thermal gradients to enhance or suppress the spin signal has been proposed and demonstrated[56] (Fig. 1f). Here, the spin signal modulation is driven by thermal drifts (Fig. 1a) in combination with an energy-dependent thermoelectric power, which result in a thermoelectric spin voltage. The observation of this phenomenon requires sufficiently large lateral thermal gradients, which can be achieved by hot carrier generation, either by electrical current flow in graphene or through tunnel barrier injection[56,57].

Spin–orbit proximity effects

Proximity effects represent a versatile approach to material design that can reach its full potential with vdW heterostructures, in which the hybridization of electronic orbitals of adjacent atomically thin layers occurs. Despite the weak nature of vdW interactions, interlayer coupling of pure tunnelling character can drastically change the energy dispersion and spin texture of the electronic band structure. For instance, in BLG such tunnelling turns the linear dispersion of low-energy excitation to a parabolic shape, in addition to other band modifications. In a trilayer structure, such as that represented in Fig. 2a, the intercalated material acquires properties from the top and bottom layers, bringing unprecedented opportunities for spintronics, particularly for imprinting a SOC or magnetic exchange interaction (MEI). SOC is ubiquitous in spintronics[10,13] (Box 1), playing a central role in spin relaxation and manipulation, CSI, anisotropic magnetoresistance, perpendicular magnetic anisotropy, spin–orbit torques (SOTs) and the emergence of topological states. Proximity SOC concepts are therefore particularly relevant, as they can potentially help engineer and control many of these phenomena.

Graphene and BLG represent model materials for proximity-effect studies. In their isolated states, the SOC strength is only tens of microelectronvolts and opens a very small spin–orbit gap, as shown by ab initio calculations[36,58,59] and recent experiments[37,60]. The Hamiltonian of isolated graphene is $H \approx H_0$, where H_0 characterizes Dirac carriers (Box 2). When graphene makes contact with other materials—2D semiconductors and 2D insulators that preserve the Dirac cones in their bandgaps are of interest—the character of H can radically change. Surprisingly generic Hamiltonian models $H = H_0 + H_{t,b}$ have been derived that capture first-principles results, where $H_{t,b}$ comprises separate orbital, spin–orbit and exchange terms (Box 2) that can be tracked back to the top and/or bottom 2D materials (Fig. 2a).

Owing to the short range of the magnetic-exchange and spin–orbit interactions, proximity effects are largely driven by the layer adjacent to the proximitized graphene. Therefore, the thickness of the 2D magnet or large-SOC material does not require control. In addition, the proximity effect in BLG predominantly develops only in the layer in contact with the material.

According to the previous discussion, it is not surprising that proximity SOC concepts are best established for graphene. Although materials such as hBN do not increase graphene's SOC beyond tens of microelectronvolts[61], it has been demonstrated that strong SOC materials (such as TMDCs or the Bi_2Se_3 TI family) significantly alter it or reinforce it (panels b and c of the figure in Box 2). The graphene Dirac cones are preserved within the bandgaps of many TMDCs[62], which allows one to exploit the advantages of graphene's high mobility and novel proximity spin interactions[63,64]. The SOC strength can reach millielectronvolts (panel b of the figure in Box 2) and be dominated by a valley Zeeman SOC, which is characterized by an out-of-plane spin–orbit field that is opposite at K and K′ valleys (as in the TMDC). In addition, carriers experience a Rashba SOC, with an in-plane spin–orbit field texture perpendicular to the momentum. On the orbital level, the breaking of the pseudospin symmetry leads to the appearance of an orbital gap, described by a staggered potential. The valley Zeeman and Rashba fields are predicted to change by twisting the graphene relative to the TMDC, with the largest SOC strength appearing at 15–20° between the lattice vectors[65,66]. Band structures at smaller twist angles have been theoretically investigated[67,68]. Graphene can also be proximitized by TIs, such as Bi_2Se_3[69–71]. These 3D TIs exhibit protected surface states with in-plane spin–orbit fields inducing spin–momentum locking. Surprisingly, the proximitized SOC is still dominated by the out-of-plane valley Zeeman coupling, which is not present in the TI (panel c of the figure in Box 2).

Experimental signatures of proximity-induced SOC in graphene–TMDC heterostructures have been found in weak (anti-) localization measurements[72–76]. However, the results are controversial in terms of the SOC strength, which ranges from ~1 to 10 meV, as well as the nature of the SOC, which was reported to have Rashba or valley Zeeman character. Variations on the SOC strength may be due in part to variations in the interface properties, twist angle or the presence of trapped bubbles—all of which are difficult to control

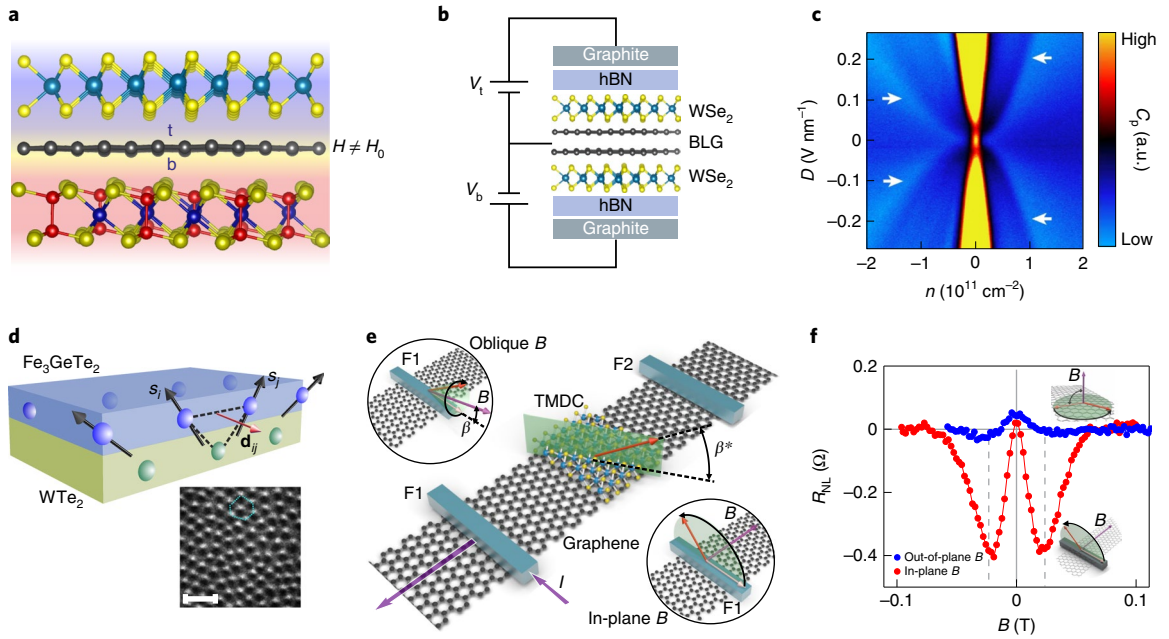

Fig. 2 | Proximity effects. a, In a trilayer vdW heterostructure, the middle layer is proximitized by the top (t) and bottom (b) layers. Its effective Hamiltonian H is distinct from the Hamiltonian H_0 of the isolated layer, acquiring properties from t and b. **b**, Device geometry to investigate proximity SOC in BLG encapsulated with WSe_2. The charge density n and displacement field D are controlled with top and bottom gates. **c**, Penetration field capacitance C_p as a function of n and D showing an incompressibility peak at $D=0$ for $n=0$. Arrows indicate maxima associated with band splitting due to proximity SOC. **d**, Illustration of the DMI at the vdW interface of a 2D magnet (Fe_3GeTe_2) and a TMDC with large SOC (WTe_2), s_i and s_j represent the spins of neighbouring atoms and $\mathbf{d}_{ij}$ the DMI vector. The interfacial DMI stabilizes magnetic skyrmions, as observed by Lorentz transmission electron microscopy in WTe_2–Fe_3GeTe_2 under a 0.51 T magnetic field (inset image; scale bar, 500 nm); one hexagonal skyrmion lattice is indicated with the turquoise dashed lines. **e**, Schematics of a lateral spin device for investigating proximity SOC in graphene by means of spin transport. The device consists of a graphene spin channel that is partially covered with a TMDC. The two attached ferromagnets (F1 and F2) act as the spin injector and detector, respectively. A charge current I through F1 injects spins with an orientation parallel to the F1 magnetization direction. While diffusing towards the spin detector (F2), the spins precess under either an oblique or in-plane magnetic field B, as represented in the top and bottom insets. When they reach the TMDC, their orientation is characterized by the angle β^*, whose value is tuned with the magnitude of B. **f**, Spin precession experiments in a graphene–WS_2 device. The non-local signal R_{NL} is shown for B perpendicular to the plane (blue) and in-plane (red); spins stay in the graphene plane and precess out of it, respectively (insets). The disparity of the curves demonstrates the highly anisotropic nature of the spin dynamics in graphene–WS_2. Figure reproduced with permission from: **d** (inset), ref. [86], under Creative Commons license CC BY 4.0 (https://creativecommons.org/licenses/by/4.0/). Figure adapted with permission from: **c**, ref. [80], Springer Nature Limited; **e**,**f**, ref. [90], Springer Nature Limited.

during device fabrication. Nonetheless, the nature of the proximity SOC has been established by means of spin relaxation anisotropy and CSI experiments, as discussed below.

Graphene proximitized by a TMDC can also exhibit an inverted band structure (panel b of the figure in Box 2), suggesting emerging topological phenomena[62,77,78] distinct from isolated graphene[79] and driven by the valley Zeeman coupling. Although the band structure remains topologically trivial, protected pseudo-helical states appear at zigzag edges of proximitized nanoribbons. An inverted band structure in BLG–WSe_2 stacks has been confirmed experimentally[80] (Fig. 2b,c). Topological quantum spin Hall phases were also predicted in proximitized BLG[81], whereas helical edge modes in BLG–WSe_2 heterostructures were recently reported[82].

Proximity SOC is becoming increasingly important in 2D materials beyond graphene. A SOC enhancement could help stabilize the anisotropy or the magnetic order of a 2D magnet. An increase in the Curie temperature T_C of Fe_3GeTe_2 (FGT) up to 400 K has been observed when grown onto Bi_2Te_3. The larger T_C in thinner FGT films on Bi_2Te_3, when the opposite trend is observed in FGT alone, suggests the presence of an interfacial effect[83], although it is unclear why a substantial T_C increase persists in relatively thick FGT films (up to tens of nanometres). Similarly, an increase in T_C was observed[84] in the Heisenberg ferromagnet V_5Se_8 when in contact with $NbSe_2$. The enhanced T_C was accompanied by a strong out-of-plane magnetic anisotropy and was attributed to the Zeeman SOC in $NbSe_2$. A large SOC together with broken inversion symmetry can also favour the antisymmetric Dzyaloshinskii–Moriya exchange interaction (DMI) and lead to topological magnetic configurations[85] (Fig. 2d). Néel-type skyrmions were observed in WTe_2–FGT using Lorentz transmission electron microscopy[86] (Fig. 2d); the large interfacial DMI energy of ~1.0 mJ m^{-2} was attributed to induced Rashba SOC.

Anisotropic spin relaxation and spin filtering. One of the first spin-device realizations combining graphene with a TMDC comprised a graphene lateral spin device partially capped with MoS_2. Using electrostatic gating, the spin current across the graphene channel was controlled between on and off states, a phenomenon attributed to spin absorption at the MoS_2 (ref. [87]). It is argued that spins could move freely between graphene and MoS_2 in the off state due to the gate-induced suppression of the Schottky barrier between graphene and MoS_2, leading to fast spin relaxation[87,88].

Further studies[89,90] reported anisotropic spin relaxation in graphene–TMDC heterostructures (where TMDC = $MoSe_2$, MoS_2 and WS_2), even in the absence of spin absorption[90]. By implementing out-of-plane spin precession techniques[47–49] (Fig. 2e,f), $\zeta = \frac{\tau_{s,\perp}}{\tau_{s,\parallel}}$ was quantified. It was observed that the in-plane spin component is

Box 2 | Emergent Hamiltonian in proximitized graphene

The emergent Hamiltonian H describing Dirac electrons in proximitized graphene comprises orbital, spin–orbit and exchange terms:

$$H = H_0 + H_\Delta + H_I + H_{VZ} + H_R + H_{PIA} + H_{EX}$$

where $H_0 = \hbar v_F(\tau k_x \sigma_x + k_y \sigma_y)$ is the low-energy graphene Hamiltonian, $\mathbf{k}$ the state wave vector and σ the pseudospin Pauli matrices. The factor τ is 1 (−1) at K (K′) valleys. $H_\Delta = \Delta\sigma_z$ describes orbital gap opening when the pseudospin symmetry is broken. Other terms include the intrinsic SOC, existing already in pristine graphene, $H_I = \lambda_I \tau \sigma_z s_z$, parameterized by λ_I, with s the spin Pauli matrices. The valley Zeeman SOC $H_{VZ} = \lambda_{VZ}\tau\sigma_0 s_z$, where strength λ_{VZ} emerges when graphene is interfaced with TMDCs or TIs, for example. The Rashba SOC $H_R = \lambda_R(\tau\sigma_x s_y - \sigma_y s_x)$ is present whenever space-inversion symmetry breaks, owing to an electric field or in heterostructures. The pseudospin inversion asymmetry (PIA) SOC $H_{PIA} = \alpha(\lambda_{PIA}\sigma_z + \Delta_{PIA})(k_x s_y - k_y s_x)$, where a is the graphene lattice constant, $\lambda_{PIA} = (\lambda_{PIA,A} + \lambda_{PIA,B})/2$ and $\Delta_{PIA} = (\lambda_{PIA,A} - \lambda_{PIA,B})/2$ with $\lambda_{PIA,A(B)}$ denoting the SOC strength in the graphene sublattice A (B).

The terms proportional to λ_{PIA} and Δ_{PIA} lead to a renormalization of the Fermi velocity and a k linear band splitting, respectively. Finally, the proximity exchange coupling $H_{EX} = \lambda_{EX} s_z + \lambda_{EX}^{AF}\sigma_z s_z$ is parameterized by λ_{EX} (λ_{EX}^{AF}) and emerges when graphene forms heterostructures with ferromagnets (antiferromagnets). Neglecting many-body effects, essentially the same Hamiltonian describes the electronic states in (proximitized) TMDCs, but instead of sublattice degrees of freedom, σ describe the valence and conduction bands[139,180]. Parts **a**–**f** of the figure present representative graphene-based heterostructures, their electronic band structure at the K (and K′) points and the most relevant parameters for each of them by fitting the ab initio results of the relaxed structures (see corresponding references for further details); E, E_F and k denote the energy, the Fermi energy and linear momentum, respectively.

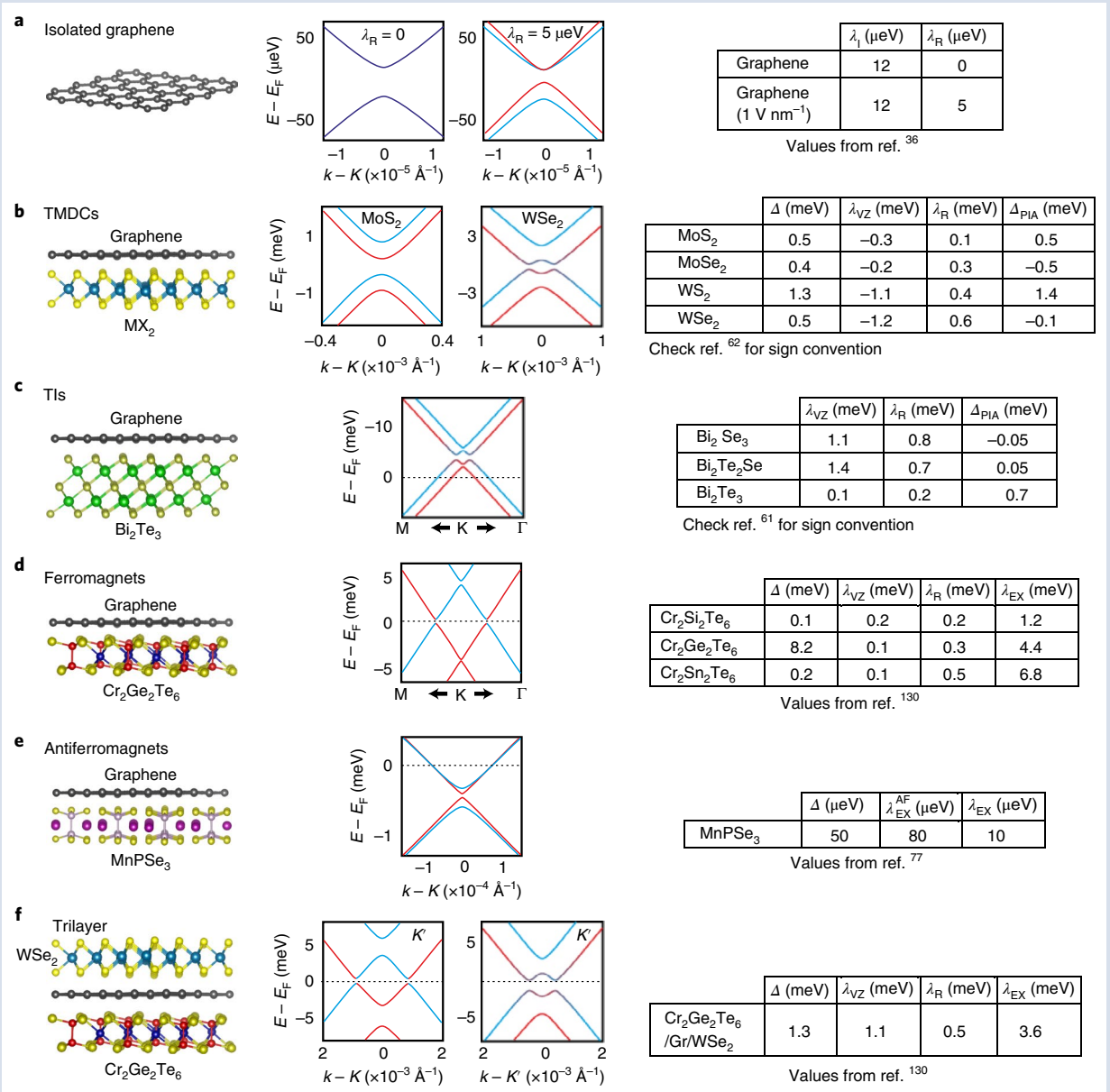

	λ_I (μeV)	λ_R (μeV)
Graphene	12	0
Graphene (1 V nm^{-1})	12	5

Values from ref. [36]

	Δ (meV)	λ_{VZ} (meV)	λ_R (meV)	Δ_{PIA} (meV)
MoS_2	0.5	−0.3	0.1	0.5
$MoSe_2$	0.4	−0.2	0.3	−0.5
WS_2	1.3	−1.1	0.4	1.4
WSe_2	0.5	−1.2	0.6	−0.1

Check ref. [62] for sign convention

	λ_{VZ} (meV)	λ_R (meV)	Δ_{PIA} (meV)
Bi_2Se_3	1.1	0.8	−0.05
Bi_2Te_2Se	1.4	0.7	0.05
Bi_2Te_3	0.1	0.2	0.7

Check ref. [61] for sign convention

	Δ (meV)	λ_{VZ} (meV)	λ_R (meV)	λ_{EX} (meV)
$Cr_2Si_2Te_6$	0.1	0.2	0.2	1.2
$Cr_2Ge_2Te_6$	8.2	0.1	0.3	4.4
$Cr_2Sn_2Te_6$	0.2	0.1	0.5	6.8

Values from ref. [130]

	Δ (μeV)	λ_{EX}^{AF} (μeV)	λ_{EX} (μeV)
$MnPSe_3$	50	80	10

Values from ref. [77]

	Δ (meV)	λ_{VZ} (meV)	λ_R (meV)	λ_{EX} (meV)
$Cr_2Ge_2Te_6$ /Gr/WSe_2	1.3	1.1	0.5	3.6

Values from ref. [130]

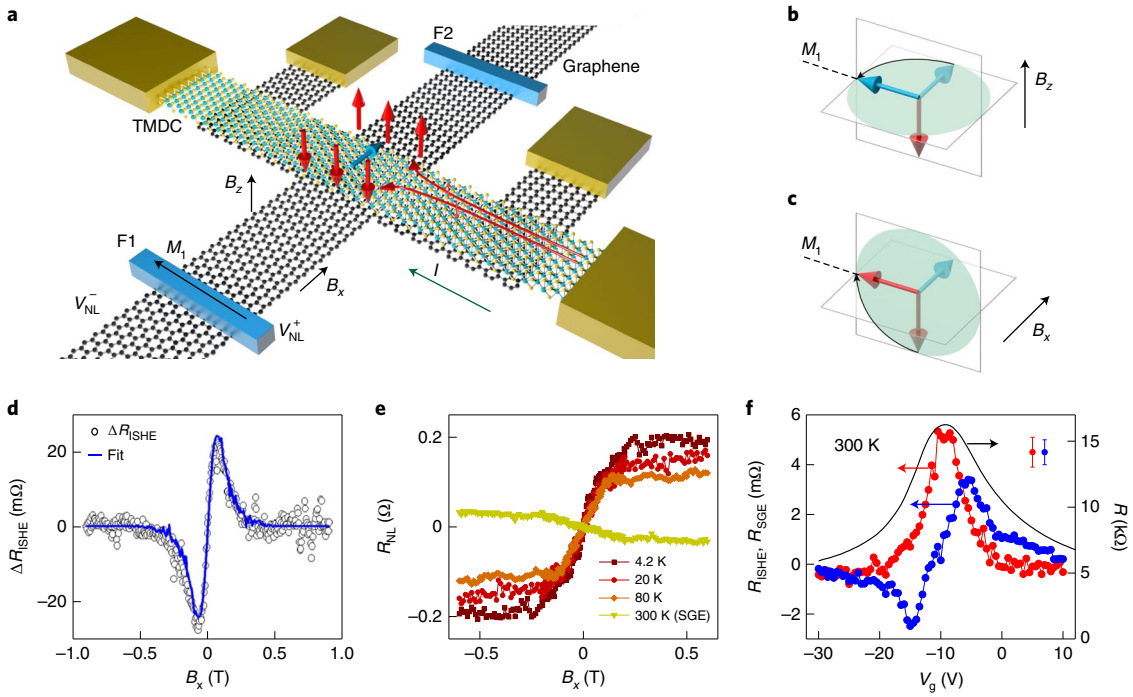

Fig. 3 | CSI in vdW heterostructures. a, Schematics of a lateral spin device for CSI experiments. The device consists of a graphene Hall cross with a TMDC covering one of the arms, which enhances the SOC in graphene. A current I along the graphene arm creates a transverse spin current with out-of-plane spin polarization driven by the SHE. Simultaneously, a non-equilibrium spin density, with in-plane spin polarization, is built at the proximitized graphene driven by the inverse SGE. Spin-sensitive contacts F1 and F2 probe diffusing spin currents under an applied magnetic field B. **b**,**c**, For B applied along z (B_z) and along x (B_x), only the spins arising from the inverse SGE (**b**) and the SHE (**c**) precess, respectively. **d**, Room-temperature inverse SHE signal ΔR_{ISHE} as a function of magnetic field B_x in a device with MoS_2 on few-layer graphene. **e**, SGE signal measured at different temperatures in a graphene–WS_2 device[103]. **f**, Experimental demonstration of the coexistence of the inverse SHE and the SGE in graphene–WS_2 at room temperature and the tunability of the measured signals R_{ISHE} (red) and R_{SGE} (blue). Here, V_g is the back-gate voltage that controls the Fermi level in graphene. The graphene resistance R is presented as a reference, showing the position of the charge neutrality point. The error bars represent twice the standard deviation of the noise distribution in the measured signals. Figure adapted with permission from: **a**–**c**,**f**, ref. [102], Springer Nature Limited; **d**, ref. [116], American Chemical Society.

strongly reduced when propagating through the graphene–TMDC region, with $\tau_{s,\parallel}$ in the range of a few picoseconds (two orders of magnitude smaller than in reference graphene devices[90]). In contrast, the out-of-plane spin component propagates much more efficiently, with $\tau_{s,\perp}$ in the range of tens of picoseconds[89,90] and thus $\zeta \approx 10$. These results evidence that graphene–TMDC heterostructures act as spin filters, whose spin transmission is tailored by the spin orientation.

When no spin current is absorbed by the TMDC, the anisotropy can be fully attributed to proximity-induced SOC[48,90]. According to theoretical predictions, the spin dynamics is controlled by the spin-valley coupling imprinted onto graphene[51]. The spin relaxation is governed by the Dyakonov–Perel mechanism, with $\tau_{s,\perp}$ and $\tau_{s,\parallel}$ largely determined by the momentum (τ_p) and intervalley (τ_{iv}) scattering times, respectively, typically with $\tau_p \ll \tau_{iv}$. Because of the relatively long τ_{iv}, the in-plane spins precess under a slowly fluctuating effective (perpendicular) magnetic field between K and K′, leading to fast spin relaxation. In contrast, because of the short τ_p, out-of-plane spins precess under fast fluctuating Rashba fields, and their relaxation is suppressed due to motional narrowing[13]. Derived from the emergent Hamiltonian (Box 2), ζ is[51,91,92]

$$\zeta = \left(\frac{\lambda_{VZ}}{ak\Delta_{PIA} \pm \lambda_R}\right)^2 \frac{\tau_{iv}}{\tau_p} + \frac{1}{2} \approx \left(\frac{\lambda_{VZ}}{\lambda_R}\right)^2 \frac{\tau_{iv}}{\tau_p} + \frac{1}{2} \qquad (1)$$

with the approximation being valid about the Dirac point or for small Δ_{PIA} (Box 2). In the absence of valley Zeeman SOC, $\zeta = \frac{1}{2}$ with out-of-plane spins relaxing faster than in-plane spins, as expected for a 2D Rashba system[44]. Using an interband tunnelling description and first-principles calculations, it has been proposed that the SOC strength can be tuned with the Fermi energy, resulting in an energy-dependent anisotropy[65,66].

Anisotropic spin relaxation has also been discussed theoretically in graphene–TI[70] and graphene–hBN heterostructures[61]. Moreover, $\zeta \approx 10$ has been measured in hBN–BLG–hBN at temperatures around 100 K near the charge neutrality point[93,94]. The spin relaxation becomes isotropic either at large enough carrier densities or at high temperatures ($\zeta \approx 1$ at room temperature). Similar to graphene–TMDC, the large ζ seems to arise from the spin-valley coupling associated to the intrinsic SOC in BLG.

CSI. CSI phenomena driven by SOC are amongst the most relevant effects in modern spintronics[95]. Their presence can reveal subtle spin–orbit interactions and spin dynamics in the investigated materials. They are also central for next-generation SOT magnetic memories (SOT-MRAM)[9,10] as well as for proposals targeting energy-efficient spin-logic architectures[96] (Box 1). CSI in 2D materials has been gaining increasing attention following the report of SOTs with non-trivial (and potentially useful) symmetries using TMDCs[97], the achievement of magnetization switching with TIs and TMDCs[98,99] and the observation of spin Hall effect (SHE) and spin galvanic effect (SGE)[100–103] (Fig. 3).

A recent surge of experiments on vdW heterostructures has been triggered by the use of graphene as a channel to transport a spin current from a ferromagnetic contact to the CSI region[104,105]. The device geometry is analogous to that developed for fully metallic systems[95],

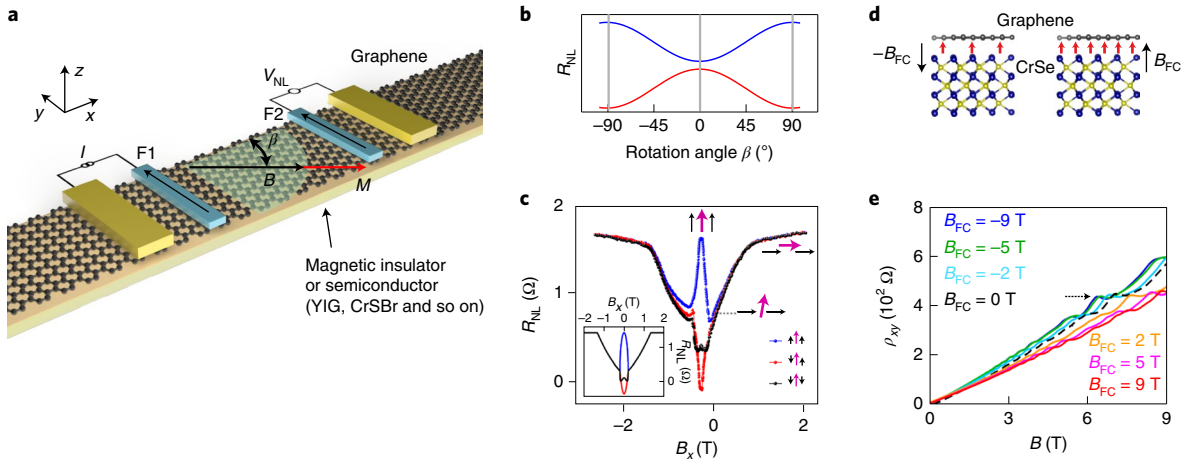

Fig. 4 | Magnetic proximity effects in graphene. a, Schematics of an experimental device to detect exchange interaction in graphene, induced by proximity of a magnetic substrate using spin transport. A magnetic field sets the orientation of the substrate magnetization and thus of the proximity-induced exchange field B_{EX} in graphene. **b**, Representation of $R_{NL} = \frac{V_{NL}}{I}$ versus β for parallel (blue) and antiparallel (red) alignment of the magnetizations of the ferromagnetic contacts F1 and F2. When $\beta = 0$, the induced exchanged magnetic field should be perpendicular to the orientation of the injected spins, and the signal should present a minimum magnitude. The coercive field of the substrate is assumed to be much lower than that of F1 and F2, as in the case of YIG. Therefore *M* follows *B* while the magnetizations of the contacts remain along their long axis (shown with black arrows in **a**). **c**, R_{NL} as a function of magnetic field along *x* (see **a**) in a graphene–CrSBr heterostructure. The initial arrangement of the magnetizations of the injector and detector contacts (black arrows) and the substrate (purple arrow) is achieved with *B* along *y*. In this case, the coercive field of the contacts is smaller than that of the substrate (an antiferromagnet). The inset shows calculated precession curves with a spin-dependent graphene conductivity model. **d**, Schematics of graphene coupled to CrSe. The red arrows represent the remanent magnetization induced at the interface by field cooling (FC) with opposite magnetic field (B_{FC}) orientations. **e**, Exchange splitting in graphene on top of antiferromagnetic CrSe. Quantum Hall plateaus in the Hall resistivity ρ_{xy} are shifted by field cooling in the heterostructure. The black arrow denotes the most pronounced plateau shifted by field cooling. The shift is attributed to the change in the remanent magnetization. Figure adapted with permission from: **c**, ref. [131], Springer Nature Limited; **e**, ref. [132], Springer Nature Limited.

consisting of a graphene Hall cross with a large-SOC 2D material along one of the arms and ferromagnetic injector and detector contacts across the other (Fig. 3a). The first experiments using platinum (Pt), a well-known material with efficient CSI by the SHE[95], demonstrated large CSI[104,105] and established the use of spin precession to investigate the nature of the CSI in 2D heterostructures[105]. The analysis and interpretation of the results differ for insulating or conducting SOC materials. Whereas in the former case it is possible to directly ascribe the CSI to proximity-induced SOC, in the latter case the overall signal can aggregate the CSI arising from proximity effects and the CSI at the surface and/or bulk of the conducting SOC material. The anomalously large CSI in graphene–Pt could be due to such aggregation of effects, although this remains to be clarified[105].

CSI driven by SOC in a vdW heterostructure was first confirmed in multilayer-graphene–MoS_2[101] (Fig. 3d). This report was soon followed by the simultaneous observations of the spin Hall effect (SHE) and spin galvanic effect (SGE) in graphene–WS_2[102,103] (Fig. 3e,f). The CSI in graphene by proximity SOC[106–108] is best established by ruling out the spin absorption in the TMDC[87,88,102]. The CSI can be controlled upon electrostatic gating, which tunes the graphene carrier density *n*. A gate-dependent CSI in proximitized graphene was observed with WS_2 up to 75 K for the inverse SGE[103] and up to room temperature for the inverse SGE and SHE (and reciprocal effects)[102]. Gate dependence of the inverse SHE and of the SGE was later reported in graphene–WSe_2, and in graphene–TaS_2 and graphene–$(Bi,Sb)_2Te_3$, respectively[109–111].

The effective conversion efficiencies compare favourably with those of metallic systems[101,102,110]. Furthermore, the experimental dependence of the CSI versus *n* in graphene–WS_2[102] agrees with theoretical modelling, for both proximity-induced SGE[107] and SHE[106]. The SOC strength has been estimated using the Kubo–Bastin formula[102,106]. By matching model calculations with the experimental results, values of $\lambda_I \approx 0.2$ meV and $\lambda_{VZ} \approx 2.2$ meV are obtained[102] (Box 2). Previous reports of SHE in graphene in proximity to WS_2 suggested a much larger SOC (17 meV)[112]. However, these experiments used the so-called H geometry[95], which in graphene devices is sensitive to a variety of phenomena that are not necessarily related to spin[5,113–115].

CSI was also investigated in other conducting 2D materials, following the same approach as used for Pt[104,105]. Experiments using 1T′-$MoTe_2$ revealed an unconventional CSI in which a charge current arises parallel to the spin orientation[116]. It is unclear whether the CSI originates in the bulk or the surface of the material. The observation is reminiscent of the appearance of unconventional SOTs in low-symmetry WTe_2[97,117], suggesting that the crystalline mirror symmetry of 1T′-$MoTe_2$ is broken, perhaps by strain introduced during device fabrication. Unconventional CSI was also observed in WTe_2 with an efficiency approaching 10%; control experiments indicate that the CSI originates in the bulk of the material[118].

Magnetic proximity effects

When non-magnetic 2D materials, such as graphene or TMDCs, are in contact with a magnetic material, they can experience a proximity-induced MEI. The induced magnetism is characterized by a net local spin polarization in equilibrium and an energy splitting of the bands, which in graphene is equal at different valleys (in the absence of SOC). The proximity MEI is parameterized by the exchange coupling strength λ_{EX} when the non-magnetic 2D material is in contact with a ferromagnet and λ_{EX}^{AF} when in contact with an antiferromagnet (Box 2). Typically, the goal is to achieve a large λ_{EX} (λ_{EX}^{AF}) while maintaining the (spin) transport capabilities of the isolated layer.

Proximity MEI in graphene. Early first-principles calculations predicted a λ_{EX} of tens of millielectronvolts in graphene when proximitized by bulk materials such as EuO[119] or the ferrimagnet $Y_3Fe_5O_{12}$

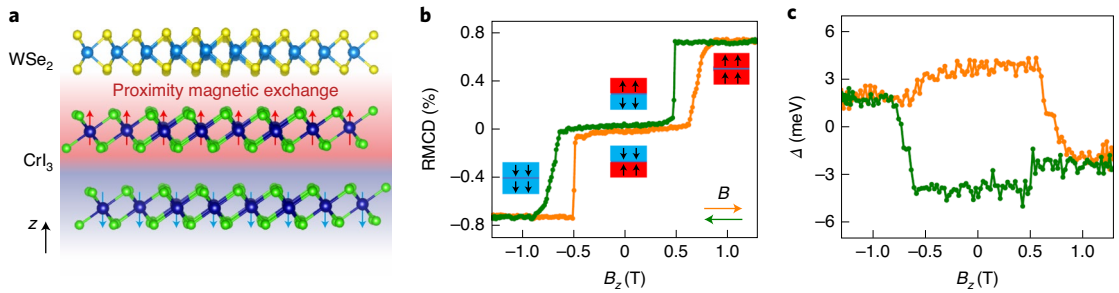

Fig. 5 | Magnetic proximity effects in TMDCs. a, Schematic of monolayer WSe_2 interfacing with a magnetic layer (CrI_3 in this case) to investigate proximity control of valley dynamics. **b**, Reflection magnetic circular dichroism (RMCD) as a function of magnetic field in WSe_2–CrI_3, showing typical features of layered antiferromagnetic bilayer CrI_3. The blue and red insets represent the magnetization orientations of the CrI_3 layers. **c**, Valley Zeeman splitting Δ as a function of magnetic field as determined from photoluminescence measurements. The legend in **b** also applies to **c**. Figure adapted with permission from: **b**,**c**, ref. [137], Springer Nature Limited.

(YIG)[120]. Similar λ_{EX} were estimated with conventional ferromagnetic metals, such as Co or Fe, across a thin hBN insulating barrier[8,121,122]. The control of proximity exchange by electrical polarization has been predicted in graphene on multiferroic $BiFeO_3$[123]. The first experimental results were also reported in graphene proximitized by bulk materials, albeit with typical λ_{EX} values that were significantly smaller than expected. Charge transport experiments in graphene–YIG showed the presence of an anomalous Hall resistance[124], whereas Zeeman SHE indicated an exchange field of up to 14 T (1.5 meV) in graphene–EuS[125]. Subsequently, spin transport experiments using lateral devices based on graphene[126] and BLG[127] on YIG provided more direct indications of proximity MEI and demonstrated spin current modulation (Fig. 4a,b), although λ_{EX} was found to be even smaller[126] (~20 μeV). Proximity MEI was also reported in YIG–graphene–hBN through non-local charge transport measurements[128], Co–graphene–NiFe junctions[129] and gate-dependent spin inversion in edge-contacted graphene spin valves[23].

The small proximity λ_{EX} observed with bulk magnets could be ascribed to rough interfaces; thus recent investigations have shifted towards proximity MEI by 2D magnets, which promise atomically smooth interfaces. Relevant 2D ferromagnets include the $Cr_2X_2Te_6$ (X = Si, Ge or Sn) or CrX_3 (X = I, Br or Cl) families with predicted λ_{EX} in the range of several millielectronvolts[130] (panel d of the figure in Box 2). The induced MEI with antiferromagnets (such as $MnPSe_3$, a 2D Heisenberg-like antiferromagnet) could lead to sub-millielectronvolt staggered exchange coupling in graphene[77] (panel e of the figure in Box 2). A few experiments do indeed indicate a substantial proximity MEI[131–133]. In graphene–CrSBr, where CrSBr is an interlayer antiferromagnet, charge and spin transport driven by electrical bias and thermal gradients[131] indicate $\lambda_{EX} \approx 20$ meV, corresponding to an exchange field of ~170 T at 4.5 K (Fig. 4c). Proximity MEI was also reported in graphene–CrSe heterostructures[132], where CrSe is a non-collinear antiferromagnet with a complex phase diagram. A magnetized interface (Fig. 4d), which does not occur in CrSe alone, is observed in graphene–CrSe by transport and magneto-optic measurements after magnetic-field cooling. The proximity exchange field was quantified using shifts in the quantum Hall plateaus and quantum oscillations (Fig. 4e), resulting in λ_{EX} larger than 130 meV at 2 K.

Proximity MEI beyond graphene. Proximity MEI has also been investigated in materials such as TMDCs and TIs. Experiments in semiconducting TMDCs typically rely on optical techniques. In WSe_2–EuS[134] and WS_2–EuS[135] heterostructures, the reflection and photoluminescence spectra of circularly polarized photons probe the electronic states of the TMDC and quantify the proximity-induced exchange splitting. For WSe_2, it was estimated that $\lambda_{EX} \approx 2$–4 meV, corresponding to an exchange field of ~10–20 T. For WS_2, the splitting was found to be much larger $\lambda_{EX} \approx 19$ meV and to have opposite sign. According to theoretical modelling[135], the magnitude and sign of the splitting is determined by the surface termination of EuS and the band alignment between TMDCs and EuS.

As with graphene, a growing number of studies are being carried out with 2D magnets[136,137]. Placing a monolayer TMDC on CrI_3 (Fig. 5a) results in an estimated exchange splitting in the millielectronvolt range[138], which should affect the exciton spectra[139]. Given its short-range interaction, the proximity effect allows the magnetization of the adjacent 2D-magnet layer to be probed, even in the absence of a global magnetic moment. A layer-dependent magnetic proximity effect has been observed in monolayer WSe_2 on few-layer CrI_3[137]. While magneto-optic measurements demonstrate that bilayer CrI_3 is a layered antiferromagnet, circularly polarized photoluminescence spectra show that the exchange splitting in WSe_2 is most sensitive to the interfacial layer. The contribution of the second layer to the splitting is of substantially smaller magnitude and has an unexpected opposite sign (Fig. 5b,c). The quantitative interpretation of the exciton spectra and dynamics is not straightforward—the hybridization of the TMDC orbitals with the spin-polarized CrI_3 orbitals is complex. In particular, it is expected that twisting the two layers would lead to variations in the proximity MEI, both in magnitude and character[138]. Furthermore, photoluminescence studies in $MoSe_2$–$CrBr_3$ uncovered a charge dependence of the proximity effects in which the valley polarization of the $MoSe_2$ trion state follows the local $CrBr_3$ magnetization, whereas the neutral exciton state is insensitive to it[140]. This is attributed to spin-dependent interlayer charge transfer on timescales between the exciton and trion radiative lifetimes.

Magnetic proximity effects are also being intensively investigated in layered 2D and 3D TIs. In the 3D TIs, such as the Bi_2Te_3 family, broken time-reversal symmetry induces a gap in the Dirac band dispersion of the surface states[141]. Tuning of the Fermi level in the gap leads to the emergence of a quantum Hall effect at zero magnetic field: the quantum anomalous Hall effect (QAHE), a phenomenon that is very promising for quantum metrology. Signatures of proximity magnetism in 3D TIs have been reported, for example, in [EuS, YIG, $Tm_3Fe_5O_{12}$, $Cr_2Ge_2Te_6$]–TI with the observation of an anomalous Hall effect[142–144] or by investigating spin-polarized neutron reflectivity[145]. However, the origin of the magnetic signals in these types of experiment is usually not fully understood[146–148]. An unambiguous demonstration of proximity MEI was reported in (Zn,Cr)Te–$(Bi,Sb)_2Te_3$–(Zn,Cr)Te heterostructures with the observation of the QAHE[149]. In 2D TIs, or quantum spin Hall insulators, such as monolayer WTe_2, the conduction is dominated by helical edge states[150,151] with canted spin orientation due to reduced

symmetries[152–154]. When WTe_2 is placed in a heterostructure with CrI_3, magnetic proximity could lead to a change in the edge state conductance that is controlled by the magnetization of the interfacial CrI_3 layer[155]. This could ultimately result in the observation of the QAHE, depending on other phenomena, such as charge transfer at the interface.

Conclusions and future perspectives

Recent progress in the design of complex vdW heterostructures brings unprecedented possibilities for developing innovative ultra-compact spin devices and computing architectures. With respect to conventional spintronic applications, it is necessary to identify the best combination of 2D materials to demonstrate practical magnetic tunnel junctions (either with conducting or insulating 2D magnets) or CSI-induced switching of 2D magnets[156] (using high spin–orbit materials such as WTe_2 and Bi_2Te_3). Voltage control of magnetic properties is another promising avenue available with 2D materials (Box 1). Advances have been made in this regard[7,157], while electric-field-dependent proximity SOC in 2D magnets will certainly bring further opportunities. In addition, the reduced symmetries in monolayer TMDCs such as $MoTe_2$ and WTe_2 lead to persistent spin textures, which result in multicomponent SHE[116,118]. In combination with externally tunable spin–orbit fields, they may enable electric control of SOTs[158].

Proximity effects can be further exploited for novel spin–orbit[159,160] or magnetic valves[161,162] comprising BLG and a large-SOC material or a 2D magnet, respectively. The interplay of two factors—the short range of the proximity effect and the layer polarization in BLG—results in layer-polarized electronic bands, and asymmetrical conduction and valence bands. Applying a transverse electric field can reverse this situation, turning the SOC (or λ_{EX}) on or off and leading to novel spintronic functionalities[13]. Another functionality is offered by intercalating BLG between 2D magnets, forming a spin valve that could resolve parallel and antiparallel magnetizations in transport[163]. Another exciting prospect is engineering both the SOC and MEI, and their interplay (panel **f** of the figure in Box 2), as in the so-called ex-so-tic vdW heterostructures[164]. In graphene, such an interplay is predicted to induce the QAHE[165], novel topological phases[77,166], proximity-based SOT[130], unique signatures of anisotropic magnetoresistance and even new functionalities based on swapping SOC and exchange, all in a single device[164]. The experimental observation of these phenomena will be key milestones in spintronics and quantum metrology.

The control of interlayer twist between layers can be further exploited to tailor the spin interactions (Box 1). For instance, the atomic stacking in the moiré pattern in twisted $CrBr_3$ bilayers modulates the proximity SOC and MEI, as revealed by spin-polarized scanning tunnelling microscopy[167]. This and other emerging phenomena could become mainstream in the forthcoming years for 2D spintronics, including the control of information transfer via magnons in 2D magnets[168,169] and topological magnetic structures such as skyrmions and Néel spin spirals, which have been already observed in FGT and FGT-based heterostructures[86,170–172] and predicted in 2D Janus materials[173].

Many of these technological prospects will require overcoming important challenges. A particularly critical one is the development of large-area stable 2D magnets with magnetic order at room temperature, using scalable stacking and growth processes. Proximity SOC has shown potential to increase T_C; similarly, an enhancement of T_C could also be achieved by coupling a 2D ferromagnet to an antiferromagnet, as in Fe_3GeTe_2–$FePS_3$ heterostructures[174]. Taking advantage of SOTs will demand a full understanding of the mechanisms for (vertical) spin transfer across heterostructures and ways to take advantage of the SOTs induced by 2D materials with reduced symmetries. Applications relying on topological phases, such as the QAHE, also require robust magnetic properties to both applied currents and high temperatures. With regards to skyrmions, many fundamental challenges lie ahead beyond material issues, such as the development of writing, processing and reading functionalities using all-electrical schemes. Moreover, increasingly realistic theoretical modelling of proximity effects in complex vdW heterostructures (combining different 2D material families) is necessary to grasp the subtle spin and exciton dynamics and to separate the contributions of the exchange interaction from spin and orbital moments. Extracting (minimum) model Hamiltonians from ab initio calculations is becoming very challenging owing to the intertwined combination of all interactions involved, which are necessary for performing spin transport simulations. Precise comparisons with experiments are hampered by the difficulty of reproducing interfaces and controlling the stacking, especially in multilayer heterostructures.

The advances covered in this Review therefore represent the starting point for 2D material design for spintronics and opto-spintronics. However, the endless possibilities offered by proximity effects promise an enduring impact in terms of innovative devices and architectures. Engineering vdW heterostructures can reveal novel classes of artificial quantum materials[175], offering opportunities for both scientific discoveries and technological breakthroughs. Information and quantum computing paradigms, electrically driven light emitters, photodetectors and sensors might emerge by harnessing the rich internal degrees of freedom of 2D materials (spin, valley, sublattice, excitonic and layer pseudospin) and the creation and manipulation of entangled states.

Received: 18 September 2020; Accepted: 3 June 2021;
Published online: 19 July 2021

References

1. Geim, A. K. & Grigorieva, I. V. Van der Waals heterostructures. *Nature* **499**, 419–425 (2013).
2. Novoselov, K. S., Mishchenko, A., Carvalho, A. & Neto, A. H. C. 2D materials and van der Waals heterostructures. *Science* **353**, aac9439 (2016).
3. Han, W., Kawakami, R. K., Gmitra, M. & Fabian, J. Graphene spintronics. *Nat. Nanotechnol.* **9**, 794–807 (2014).
4. Roche, S. et al. Graphene spintronics: the European Flagship perspective. *2D Mater.* **2**, 030202 (2015).
5. Avsar, A. et al. Colloquium: spintronics in graphene and other two-dimensional materials. *Rev. Mod. Phys.* **92**, 021003 (2020).
6. Manzeli, S., Ovchinnikov, D., Pasquier, D., Yazyev, O. V. & Kis, A. 2D transition metal dichalcogenides. *Nat. Rev. Mater.* **2**, 17033 (2017).
7. Gibertini, M., Koperski, M., Morpurgo, A. F. & Novoselov, K. S. Magnetic 2D materials and heterostructures. *Nat. Nanotechnol.* **14**, 408–419 (2019).
8. Zutic, I., Matos-Abiague, A., Scharf, B., Dery, H. & Belaschhenko, K. Proximitized materials. *Mater. Today* **22**, 85–107 (2019).
9. Manchon, A. et al. Current-induced spin-orbit torques in ferromagnetic and antiferromagnetic systems. *Rev. Mod. Phys.* **91**, 035004 (2019).
10. Dieny, B. et al. Opportunities and challenges for spintronics in the microelectronics industry. *Nat. Electron.* **3**, 446–459 (2020).
11. Loong, L. M. et al. Flexible MgO barrier magnetic tunnel junctions. *Adv. Mater.* **28**, 4983–4990 (2016).
12. Serrano, I. G. et al. Two-dimensional flexible high diffusive spin circuits. *Nano Lett.* **19**, 666–673 (2019).
13. Žutić, I., Fabian, J. & Das Sarma, S. Spintronics: fundamentals and applications. *Rev. Mod. Phys.* **76**, 323–410 (2004).
14. Schmidt, G., Ferrand, D., Molenkamp, L. W., Filip, A. T. & van Wees, B. J. Fundamental obstacle for electrical spin injection from a ferromagnetic metal into a diffusive semiconductor. *Phys. Rev. B* **62**, R4790–R4793 (2000).
15. Tombros, N., Jozsa, C., Popinciuc, M., Jonkman, H. T. & van Wees, B. J. Electronic spin transport and spin precession in single graphene layers at room temperature. *Nature* **448**, 571–574 (2007).
16. Han, W. et al. Tunneling spin injection into single layer graphene. *Phys. Rev. Lett.* **105**, 167202 (2010).
17. Neumann, I., Costache, M. V., Bridoux, G., Sierra, J. F. & Valenzuela, S. O. Enhanced spin accumulation at room temperature in graphene spin valves with amorphous carbon interfacial layers. *Appl. Phys. Lett.* **103**, 112401 (2013).
18. Singh, S. et al. Strontium oxide tunnel barriers for high quality spin transport and large spin accumulation in graphene. *Nano Lett.* **17**, 7578–7585 (2017).

19. Friedman, A. L., van 't Erve, O. M. J., Li, C. H., Robinson, J. T. & Jonker, B. T. Homoepitaxial tunnel barriers with functionalized graphene-on-graphene for charge and spin transport. *Nat. Commun.* **5**, 3161 (2014).
20. Kamalakar, M. V., Dankert, A., Bergsten, J., Ive, T. & Dash, S. P. Enhanced tunnel spin injection into graphene using chemical vapor deposited hexagonal boron nitride. *Sci. Rep.* **4**, 6146 (2014).
21. Gurram, M., Omar, S. & van Wees, B. J. Bias induced up to 100% spin-injection and detection polarizations in ferromagnet/bilayer-hBN/graphene/hBN heterostructures. *Nat. Commun.* **8**, 248 (2017).
22. Avsar, A. et al. Gate-tunable black phosphorus spin valve with nanosecond spin lifetimes. *Nat. Phys.* **13**, 888–893 (2017).
23. Xu, J. et al. Spin inversion in graphene spin valves by gate-tunable magnetic proximity effect at one-dimensional contacts. *Nat. Commun.* **9**, 2869 (2018).
24. Yang, L. et al. Long-lived nanosecond spin relaxation and spin coherence of electrons in monolayer MoS_2 and WS_2. *Nat. Phys.* **11**, 830–834 (2015).
25. Dey, P. et al. Gate-controlled spin-valley locking of resident carriers in WS_2 monolayers. *Phys. Rev. Lett.* **119**, 137401 (2017).
26. Kim, J. et al. Observation of ultralong valley lifetime in WSe_2/MoS_2 heterostructures. *Sci. Adv.* **3**, e1700518 (2017).
27. Gmitra, M. & Fabian, J. Graphene on transition-metal dichalcogenides: a platform for proximity spin-orbit physics and optospintronics. *Phys. Rev. B* **92**, 155403 (2015).
28. Luo, Y. K. et al. Opto-valleytronic spin injection in monolayer MoS_2/few-layer graphene hybrid spin valves. *Nano Lett.* **17**, 3877–3883 (2017).
29. Avsar, A. et al. Optospintronics in graphene via proximity coupling. *ACS Nano* **11**, 11678–11686 (2017).
30. Drögeler, M. et al. Spin lifetimes exceeding 12 ns in graphene nonlocal spin valve devices. *Nano Lett.* **16**, 3533–3539 (2016).
31. Gebeyehu, Z. M. et al. Spin communication over 30-μm long channels of chemical vapor deposited graphene on SiO_2. *2D Mater.* **6**, 034003 (2019).
32. McCormick, E. J. et al. Imaging spin dynamics in monolayer WS_2 by time-resolved Kerr rotation microscopy. *2D Mater.* **5**, 011010 (2017).
33. Song, X., Xie, S., Kang, K., Park, J. & Sih, V. Long-lived hole spin/valley polarization probed by Kerr rotation in monolayer WSe_2. *Nano Lett.* **16**, 5010–5014 (2016).
34. Ersfeld, M. et al. Spin states protected from intrinsic electron–phonon coupling reaching 100 ns lifetime at room temperature in $MoSe_2$. *Nano Lett.* **19**, 4083–4090 (2019).
35. Jin, C. et al. Imaging of pure spin-valley diffusion current in WS_2-WSe_2 heterostructures. *Science* **360**, 893–896 (2018).
36. Gmitra, M., Konschuh, S., Ertler, C., Ambrosch-Draxl, C. & Fabian, J. Band-structure topologies of graphene: spin-orbit coupling effects from first principles. *Phys. Rev. B* **80**, 235431 (2009).
37. Sichau, J. et al. Resonance microwave measurements of an intrinsic spin-orbit coupling gap in graphene: a possible indication of a topological state. *Phys. Rev. Lett.* **122**, 046403 (2019).
38. Kochan, D., Gmitra, M. & Fabian, J. Spin relaxation mechanism in graphene: resonant scattering by magnetic impurities. *Phys. Rev. Lett.* **112**, 116602 (2014).
39. Kochan, D., Irmer, S., Gmitra, M. & Fabian, J. Resonant scattering by magnetic impurities as a model for spin relaxation in bilayer graphene. *Phys. Rev. Lett.* **115**, 196601 (2015).
40. Van Tuan, D., Ortmann, F., Soriano, D., Valenzuela, S. O. & Roche, S. Pseudospin-driven spin relaxation mechanism in graphene. *Nat. Phys.* **10**, 857–863 (2014).
41. Cummings, A. W. & Roche, S. Effects of dephasing on spin lifetime in ballistic spin-orbit materials. *Phys. Rev. Lett.* **116**, 086602 (2016).
42. Ochoa, H., Castro Neto, A. H. & Guinea, F. Elliot-Yafet mechanism in graphene. *Phys. Rev. Lett.* **108**, 206808 (2012).
43. Zhang, P. & Wu, M. W. Electron spin relaxation in graphene with random Rashba field: comparison of the D'yakonov–Perel' and Elliott–Yafet-like mechanisms. *N. J. Phys.* **14**, 033015 (2012).
44. Fabian, J., Matos-Abiague, A., Ertler, C. & Zutic, I. Semiconductor spintronics. *Acta Phys. Slov.* **57**, 565–907 (2007).
45. Vila, M. et al. Nonlocal spin dynamics in the crossover from diffusive to ballistic transport. *Phys. Rev. Lett.* **124**, 196602 (2020).
46. Guimarães, M. H. D. et al. Controlling spin relaxation in hexagonal bn-encapsulated graphene with a transverse electric field. *Phys. Rev. Lett.* **113**, 086602 (2014).
47. Raes, B. et al. Determination of the spin-lifetime anisotropy in graphene using oblique spin precession. *Nat. Commun.* **7**, 11444 (2016).
48. Benítez, L. A. et al. Investigating the spin-orbit interaction in van der Waals heterostructures by means of the spin relaxation anisotropy. *APL Mater.* **7**, 120701 (2019).
49. Raes, B. et al. Spin precession in anisotropic media. *Phys. Rev. B* **95**, 085403 (2017).
50. Ringer, S. et al. Measuring anisotropic spin relaxation in graphene. *Phys. Rev. B* **97**, 205439 (2018).
51. Cummings, A. W., Garcia, J. H., Fabian, J. & Roche, S. Giant spin lifetime anisotropy in graphene induced by proximity effects. *Phys. Rev. Lett.* **119**, 206601 (2017).
52. Behin-Aein, B., Datta, D., Salahuddin, S. & Datta, S. Proposal for an all-spin logic device with built-in memory. *Nat. Nanotechnol.* **5**, 266–270 (2010).
53. Wen, H. et al. Experimental demonstration of XOR operation in graphene magnetologic gates at room temperature. *Phys. Rev. Appl.* **5**, 044003 (2016).
54. Lin, X. et al. Gate-driven pure spin current in graphene. *Phys. Rev. Appl.* **8**, 034006 (2017).
55. Ingla-Aynés, j., Meijerink, R. J. & van Wees, B. J. Eighty-eight percent directional guiding of spin currents with 90 μm relaxation length in bilayer graphene using carrier drift. *Nano Lett.* **16**, 4825–4830 (2016).
56. Sierra, J. F. et al. Thermoelectric spin voltage in graphene. *Nat. Nanotechnol.* **13**, 107–111 (2018).
57. Sierra, J. F., Neumann, I., Costache, M. V. & Valenzuela, S. O. Hot-carrier Seebeck effect: diffusion and remote detection of hot carriers in graphene. *Nano Lett.* **15**, 4000–4005 (2015).
58. Abdelouahed, S., Ernst, A., Henk, J., Maznichenko, I. V. & Mertig, I. Spin-split electronic states in graphene: effects due to lattice deformation, Rashba effect, and adatoms by first principles. *Phys. Rev. B* **82**, 125424 (2010).
59. Konschuh, S., Gmitra, M., Kochan, D. & Fabian, J. Theory of spin-orbit coupling in bilayer graphene. *Phys. Rev. B* **85**, 115423 (2012).
60. Banszerus, L. et al. Observation of the spin-orbit gap in bilayer graphene by one-dimensional ballistic transport. *Phys. Rev. Lett.* **124**, 177701 (2020).
61. Zollner, K., Gmitra, M. & Fabian, J. Heterostructures of graphene and hBN: electronic, spin-orbit, and spin relaxation properties from first principles. *Phys. Rev. B* **99**, 125151 (2019).
62. Gmitra, M., Kochan, D., Högl, P. & Fabian, J. Trivial and inverted Dirac bands and the emergence of quantum spin Hall states in graphene on transition-metal dichalcogenides. *Phys. Rev. B* **93**, 155104 (2016).
63. Kochan, D., Irmer, S. & Fabian, J. Model spin-orbit coupling Hamiltonians for graphene systems. *Phys. Rev. B* **95**, 165415 (2017).
64. Rossi, E. & Triola, C. Van Der Waals heterostructures with spin-orbit coupling. *Ann. Phys.* **532**, 1900344 (2020).
65. Li, Y. & Koshino, M. Twist-angle dependence of the proximity spin-orbit coupling in graphene on transition-metal dichalcogenides. *Phys. Rev. B* **99**, 075438 (2019).
66. David, A. Induced spin-orbit coupling in twisted graphene–transition metal dichalcogenide heterobilayers: twistronics meets spintronics. *Phys. Rev. B* **100**, 085412 (2019).
67. Alsharari, A. M., Asmar, M. M. & Ulloa, S. E. Topological phases and twisting of graphene on a dichalcogenide monolayer. *Phys. Rev. B* **98**, 195129 (2018).
68. Wang, T., Bultinck, N. & Zaletel, M. P. Flat-band topology of magic angle graphene on a transition metal dichalcogenide. *Phys. Rev. B* **102**, 235146 (2020).
69. Zollner, K. & Fabian, J. Heterostructures of graphene and topological insulators Bi_2Se_3, Bi_2Te_3, and Sb_2Te_3. *Phys. Stat. Solidi B* **258**, 2000081 (2021).
70. Song, K. et al. Spin proximity effects in graphene/topological insulator heterostructures. *Nano Lett.* **18**, 2033–2039 (2018).
71. Zollner, K. & Fabian, J. Single and bilayer graphene on the topological insulator Bi_2Se_3: electronic and spin-orbit properties from first principles. *Phys. Rev. B* **100**, 165141 (2019).
72. Wang, Z. et al. Strong interface-induced spin–orbit interaction in graphene on WS_2. *Nat. Commun.* **6**, 8339 (2015).
73. Wang, Z. et al. Origin and magnitude of 'designer' spin-orbit interaction in graphene on semiconducting transition metal dichalcogenides. *Phys. Rev. X* **6**, 041020 (2016).
74. Yang, B. et al. Tunable spin–orbit coupling and symmetry-protected edge states in graphene/WS_2. *2D Mater.* **3**, 031012 (2016).
75. Völkl, T. et al. Magnetotransport in heterostructures of transition metal dichalcogenides and graphene. *Phys. Rev. B* **96**, 125405 (2017).
76. Zihlmann, S. et al. Large spin relaxation anisotropy and valley-Zeeman spin-orbit coupling in WSe_2/graphene/h-BN heterostructures. *Phys. Rev. B* **97**, 075434 (2018).
77. Högl, P. et al. Quantum anomalous Hall effects in graphene from proximity-induced uniform and staggered spin-orbit and exchange coupling. *Phys. Rev. Lett.* **124**, 136403 (2020).
78. Frank, T., Högl, P., Gmitra, M., Kochan, D. & Fabian, J. Protected pseudohelical edge states in Z_2-trivial proximitized graphene. *Phys. Rev. Lett.* **120**, 156402 (2018).
79. Kane, C. L. & Mele, E. J. Quantum spin Hall effect in graphene. *Phys. Rev. Lett.* **95**, 226801 (2005).
80. Island, J. O. et al. Spin–orbit-driven band inversion in bilayer graphene by the van der Waals proximity effect. *Nature* **571**, 85–89 (2019).

81. Alsharari, A. M., Asmar, M. M. & Ulloa, S. E. Proximity-induced topological phases in bilayer graphene. *Phys. Rev. B* **97**, 241104 (2018).
82. Tiwari, P., Srivastav, S. K., Ray, S., Das, T. & Bid, A. Observation of time-reversal invariant helical edge-modes in bilayer graphene/WSe_2 heterostructure. *ACS Nano* **15**, 916–922 (2021).
83. Wang, H. et al. Above room-temperature ferromagnetism in wafer-scale two-dimensional van der Waals Fe_3GeTe_2 tailored by a topological insulator. *ACS Nano* **14**, 10045–10053 (2020).
84. Matsuoka, H. et al. Spin–orbit-induced Ising ferromagnetism at a van der Waals Interface. *Nano Lett.* **21**, 1807–1814 (2021).
85. Fert, A., Reyren, N. & Cros, V. Magnetic skyrmions: advances in physics and potential applications. *Nat. Rev. Mater.* **2**, 1–15 (2017).
86. Wu, Y. et al. Néel-type skyrmion in WTe_2 /Fe_3GeTe_2 van der Waals heterostructure. *Nat. Commun.* **11**, 3860 (2020).
87. Yan, W. et al. A two-dimensional spin field-effect switch. *Nat. Commun.* **7**, 13372 (2016).
88. Dankert, A. & Dash, S. P. Electrical gate control of spin current in van der Waals heterostructures at room temperature. *Nat. Commun.* **8**, 16093 (2017).
89. Ghiasi, T. S., Ingla-Aynés, J., Kaverzin, A. A. & van Wees, B. J. Large proximity-induced spin lifetime anisotropy in transition-metal dichalcogenide/graphene heterostructures. *Nano Lett.* **17**, 7528–7532 (2017).
90. Benítez, L. A. et al. Strongly anisotropic spin relaxation in graphene–transition metal dichalcogenide heterostructures at room temperature. *Nat. Phys.* **14**, 303–308 (2018).
91. Offidani, M. & Ferreira, A. Microscopic theory of spin relaxation anisotropy in graphene with proximity-induced spin–orbit coupling. *Phys. Rev. B* **98**, 245408 (2018).
92. Garcia, J. H., Vila, M., Cummings, A. W. & Roche, S. Spin transport in graphene/transition metal dichalcogenide heterostructures. *Chem. Soc. Rev.* **47**, 3359–3379 (2018).
93. Xu, J., Zhu, T., Luo, Y. K., Lu, Y.-M. & Kawakami, R. K. Strong and tunable spin-lifetime anisotropy in dual-gated bilayer graphene. *Phys. Rev. Lett.* **121**, 127703 (2018).
94. Leutenantsmeyer, J. C., Ingla-Aynés, J., Fabian, J. & van Wees, B. J. Observation of spin-valley-coupling-induced large spin-lifetime anisotropy in bilayer graphene. *Phys. Rev. Lett.* **121**, 127702 (2018).
95. Sinova, J., Valenzuela, S. O., Wunderlich, J., Back, C. H. & Jungwirth, T. Spin Hall effects. *Rev. Mod. Phys.* **87**, 1213–1260 (2015).
96. Manipatruni, S. et al. Scalable energy-efficient magnetoelectric spin–orbit logic. *Nature* **565**, 35–42 (2019).
97. MacNeill, D. et al. Control of spin–orbit torques through crystal symmetry in WTe_2/ferromagnet bilayers. *Nat. Phys.* **13**, 300–305 (2017).
98. Shi, S. et al. All-electric magnetization switching and Dzyaloshinskii–Moriya interaction in WTe_2/ferromagnet heterostructures. *Nat. Nanotechnol.* **14**, 945–949 (2019).
99. Liang, S. et al. Spin-orbit torque magnetization switching in $MoTe_2$/permalloy heterostructures. *Adv. Mater.* **32**, 2002799 (2020).
100. Dushenko, S. et al. Gate-tunable spin-charge conversion and the role of spin-orbit interaction in graphene. *Phys. Rev. Lett.* **116**, 166102 (2016).
101. Safeer, C. K. et al. Room-temperature spin Hall effect in graphene/MoS_2 van der Waals heterostructures. *Nano Lett.* **19**, 1074–1082 (2019).
102. Benítez, L. A. et al. Tunable room-temperature spin galvanic and spin Hall effects in van der Waals heterostructures. *Nat. Mater.* **19**, 170–175 (2020).
103. Ghiasi, T. S., Kaverzin, A. A., Blah, P. J. & van Wees, B. J. Charge-to-spin conversion by the Rashba–Edelstein effect in two-dimensional van der Waals heterostructures up to room temperature. *Nano Lett.* **19**, 5959–5966 (2019).
104. Yan, W. et al. Large room temperature spin-to-charge conversion signals in a few-layer graphene/Pt lateral heterostructure. *Nat. Commun.* **8**, 661 (2017).
105. Savero Torres, W. et al. Spin precession and spin Hall effect in monolayer graphene/Pt nanostructures. *2D Mater.* **4**, 041008 (2017).
106. Garcia, J. H., Cummings, A. W. & Roche, S. Spin Hall effect and weak antilocalization in graphene/transition metal dichalcogenide heterostructures. *Nano Lett.* **17**, 5078–5083 (2017).
107. Offidani, M., Milletarì, M., Raimondi, R. & Ferreira, A. Optimal charge-to-spin conversion in graphene on transition-metal dichalcogenides. *Phys. Rev. Lett.* **119**, 196801 (2017).
108. Milletarì, M., Offidani, M., Ferreira, A. & Raimondi, R. Covariant conservation laws and the spin Hall effect in Dirac-Rashba systems. *Phys. Rev. Lett.* **119**, 246801 (2017).
109. Li, L. et al. Gate-tunable reversible Rashba–Edelstein effect in a few-layer graphene/2H-TaS_2 heterostructure at room temperature. *ACS Nano* **14**, 5251–5259 (2020).
110. Herling, F. et al. Gate tunability of highly efficient spin-to-charge conversion by spin Hall effect in graphene proximitized with WSe_2. *APL Mater.* **8**, 071103 (2020).
111. Khokhriakov, D., Hoque, A. M., Karpiak, B. & Dash, S. P. Gate-tunable spin-galvanic effect in graphene-topological insulator van der Waals heterostructures at room temperature. *Nat. Commun.* **11**, 3657 (2020).
112. Avsar, A. et al. Spin–orbit proximity effect in graphene. *Nat. Commun.* **5**, 4875 (2014).
113. Van Tuan, D. et al. Spin Hall effect and origins of nonlocal resistance in adatom-decorated graphene. *Phys. Rev. Lett.* **117**, 176602 (2016).
114. Ribeiro, M., Power, S. R., Roche, S., Hueso, L. E. & Casanova, F. Scale-invariant large nonlocality in polycrystalline graphene. *Nat. Commun.* **8**, 2198 (2017).
115. Völkl, T. et al. Absence of a giant spin Hall effect in plasma-hydrogenated graphene. *Phys. Rev. B* **99**, 085401 (2019).
116. Safeer, C. K. et al. Large multidirectional spin-to-charge conversion in low-symmetry semimetal $MoTe_2$ at room temperature. *Nano Lett.* **19**, 8758–8766 (2019).
117. Li, P. et al. Spin-momentum locking and spin-orbit torques in magnetic nano-heterojunctions composed of Weyl semimetal WTe_2. *Nat. Commun.* **9**, 3990 (2018).
118. Zhao, B. et al. Unconventional charge–spin conversion in Weyl-semimetal WTe_2. *Adv. Mater.* **32**, 2000818 (2020).
119. Yang, H. X. et al. Proximity effects induced in graphene by magnetic insulators: first-principles calculations on spin filtering and exchange-splitting gaps. *Phys. Rev. Lett.* **110**, 046603 (2013).
120. Hallal, A., Ibrahim, F., Yang, H., Roche, S. & Chshiev, M. Tailoring magnetic insulator proximity effects in graphene: first-principles calculations. *2D Mater.* **4**, 025074 (2017).
121. Zollner, K., Gmitra, M., Frank, T. & Fabian, J. Theory of proximity-induced exchange coupling in graphene on hBN/(Co, Ni). *Phys. Rev. B* **94**, 155441 (2016).
122. Lazić, P., Belashchenko, K. D. & Žutić, I. Effective gating and tunable magnetic proximity effects in two-dimensional heterostructures. *Phys. Rev. B* **93**, 241401 (2016).
123. Ibrahim, F. et al. Unveiling multiferroic proximity effect in graphene. *2D Mater.* **7**, 015020 (2019).
124. Wang, Z., Tang, C., Sachs, R., Barlas, Y. & Shi, J. Proximity-induced ferromagnetism in graphene revealed by the anomalous Hall effect. *Phys. Rev. Lett.* **114**, 016603 (2015).
125. Wei, P. et al. Strong interfacial exchange field in the graphene/EuS heterostructure. *Nat. Mater.* **15**, 711–716 (2016).
126. Leutenantsmeyer, J. C., Kaverzin, A. A., Wojtaszek, M. & van Wees, B. J. Proximity induced room temperature ferromagnetism in graphene probed with spin currents. *2D Mater.* **4**, 014001 (2017).
127. Singh, S. et al. Strong modulation of spin currents in bilayer graphene by static and fluctuating proximity exchange fields. *Phys. Rev. Lett.* **118**, 187201 (2017).
128. Tang, C. et al. Approaching quantum anomalous Hall effect in proximity-coupled YIG/graphene/h-BN sandwich structure. *APL Mater.* **6**, 026401 (2017).
129. Asshoff, P. U. et al. Magnetoresistance of vertical Co-graphene-NiFe junctions controlled by charge transfer and proximity-induced spin splitting in graphene. *2D Mater.* **4**, 031004 (2017).
130. Zollner, K. et al. Scattering-induced and highly tunable by gate damping-like spin-orbit torque in graphene doubly proximitized by two-dimensional magnet $Cr_2Ge_2Te_6$ and monolayer WSe_2. *Phys. Rev. Res.* **2**, 043057 (2020).
131. Ghiasi, T. S. et al. Electrical and thermal generation of spin currents by magnetic bilayer graphene. *Nat. Nanotechnol.* https://doi.org/10.1038/s41565-021-00887-3 (2021).
132. Wu, Y. et al. Large exchange splitting in monolayer graphene magnetized by an antiferromagnet. *Nat. Electron.* **3**, 604–611 (2020).
133. Ghazaryan, D. et al. Magnon-assisted tunnelling in van der Waals heterostructures based on $CrBr_3$. *Nat. Electron.* **1**, 344–349 (2018).
134. Zhao, C. et al. Enhanced valley splitting in monolayer WSe_2 due to magnetic exchange field. *Nat. Nanotechnol.* **12**, 757–762 (2017).
135. Norden, T. et al. Giant valley splitting in monolayer WS_2 by magnetic proximity effect. *Nat. Commun.* **10**, 4163 (2019).
136. Zhong, D. et al. Van der Waals engineering of ferromagnetic semiconductor heterostructures for spin and valleytronics. *Sci. Adv.* **3**, e1603113 (2017).
137. Zhong, D. et al. Layer-resolved magnetic proximity effect in van der Waals heterostructures. *Nat. Nanotechnol.* **15**, 187–191 (2020).
138. Zollner, K., Faria Junior, P. E. & Fabian, J. Proximity exchange effects in $MoSe_2$ and WSe_2 heterostructures with CrI_3: twist angle, layer, and gate dependence. *Phys. Rev. B* **100**, 085128 (2019).
139. Scharf, B., Xu, G., Matos-Abiague, A. & Žutić, I. Magnetic proximity effects in transition-metal dichalcogenides: converting excitons. *Phys. Rev. Lett.* **119**, 127403 (2017).
140. Lyons, T. P. et al. Interplay between spin proximity effect and charge-dependent exciton dynamics in $MoSe_2$/$CrBr_3$ van der Waals heterostructures. *Nat. Commun.* **11**, 6021 (2020).
141. Bhattacharyya, S. et al. Recent progress in proximity coupling of magnetism to topological insulators. Preprint at https://arxiv.org/abs/2012.11248 (2020).

142. Jiang, Z. et al. Independent tuning of electronic properties and induced ferromagnetism in topological insulators with heterostructure approach. *Nano Lett.* **15**, 5835–5840 (2015).
143. Tang, C. et al. Above 400-K robust perpendicular ferromagnetic phase in a topological insulator. *Sci. Adv.* **3**, e1700307 (2017).
144. Mogi, M. et al. Current-induced switching of proximity-induced ferromagnetic surface states in a topological insulator. *Nat. Commun.* **12**, 1404 (2021).
145. Katmis, F. et al. A high-temperature ferromagnetic topological insulating phase by proximity coupling. *Nature* **533**, 513–516 (2016).
146. Krieger, J. A. et al. Do topology and ferromagnetism cooperate at the EuS/Bi_2Se_3 interface? *Phys. Rev. B* **99**, 064423 (2019).
147. Pereira, V. M. et al. Topological insulator interfaced with ferromagnetic insulators: Bi_2Te_3 thin films on magnetite and iron garnets. *Phys. Rev. Mater.* **4**, 064202 (2020).
148. Figueroa, A. I. et al. Absence of magnetic proximity effect at the interface of Bi_2Se_3 and $(Bi,Sb)_2Te_3$ with EuS. *Phys. Rev. Lett.* **125**, 226801 (2020).
149. Watanabe, R. et al. Quantum anomalous Hall effect driven by magnetic proximity coupling in all-telluride based heterostructure. *Appl. Phys. Lett.* **115**, 102403 (2019).
150. Fei, Z. et al. Edge conduction in monolayer WTe_2. *Nat. Phys.* **13**, 677–682 (2017).
151. Tang, S. et al. Quantum spin Hall state in monolayer 1T′-WTe_2. *Nat. Phys.* **13**, 683–687 (2017).
152. Garcia, J. H. et al. Canted persistent spin texture and quantum spin Hall effect in WTe_2. *Phys. Rev. Lett.* **125**, 256603 (2020).
153. Zhao, W. et al. Determination of the helical edge and bulk spin axis in quantum spin Hall insulator WTe_2. Preprint at https://arxiv.org/abs/2010.09986 (2020).
154. Tan, C. et al. Determination of the spin orientation of helical electrons in monolayer WTe_2. Preprint at https://arxiv.org/abs/2010.15717 (2020).
155. Zhao, W. et al. Magnetic proximity and nonreciprocal current switching in a monolayer WTe_2 helical edge. *Nat. Mater.* **19**, 503–507 (2020).
156. Alghamdi, M. et al. Highly efficient spin–orbit torque and switching of layered ferromagnet Fe_3GeTe_2. *Nano Lett.* **19**, 4400–4405 (2019).
157. Mak, K. F., Shan, J. & Ralph, D. C. Probing and controlling magnetic states in 2D layered magnetic materials. *Nat. Rev. Phys.* **1**, 646–661 (2019).
158. Dolui, K. et al. Proximity spin–orbit torque on a two-dimensional magnet within van der Waals heterostructure: current-driven antiferromagnet-to-ferromagnet reversible nonequilibrium phase transition in bilayer CrI_3. *Nano Lett.* **20**, 2288–2295 (2020).
159. Gmitra, M. & Fabian, J. Proximity effects in bilayer graphene on monolayer WSe_2: field-effect spin valley locking, spin-orbit valve, and spin transistor. *Phys. Rev. Lett.* **119**, 146401 (2017).
160. Khoo, J. Y., Morpurgo, A. F. & Levitov, L. On-demand spin–orbit interaction from which-layer tunability in bilayer graphene. *Nano Lett.* **17**, 7003–7008 (2017).
161. Michetti, P., Recher, P. & Iannaccone, G. Electric field control of spin rotation in bilayer graphene. *Nano Lett.* **10**, 4463–4469 (2010).
162. Zollner, K., Gmitra, M. & Fabian, J. Electrically tunable exchange splitting in bilayer graphene on monolayer $Cr_2X_2Te_6$ with X = Ge, Si, and Sn. *N. J. Phys.* **20**, 073007 (2018).
163. Cardoso, C., Soriano, D., García-Martínez, N. A. & Fernández-Rossier, J. Van der Waals spin valves. *Phys. Rev. Lett.* **121**, 067701 (2018).
164. Zollner, K., Gmitra, M. & Fabian, J. Swapping exchange and spin-orbit coupling in 2D van der Waals heterostructures. *Phys. Rev. Lett.* **125**, 196402 (2020).
165. Liu, C.-X., Zhang, S.-C. & Qi, X.-L. The quantum anomalous Hall effect: theory and experiment. *Annu. Rev. Condens. Matter Phys.* **7**, 301–321 (2016).
166. Zhang, J., Zhao, B., Yao, Y. & Yang, Z. Robust quantum anomalous Hall effect in graphene-based van der Waals heterostructures. *Phys. Rev. B* **92**, 165418 (2015).
167. Chen, W. et al. Direct observation of van der Waals stacking–dependent interlayer magnetism. *Science* **366**, 983–987 (2019).
168. Xing, W. et al. Magnon transport in quasi-two-dimensional van der Waals antiferromagnets. *Phys. Rev. X* **9**, 011026 (2019).
169. Liu, T. et al. Spin caloritronics in a $CrBr_3$ magnetic van der Waals heterostructure. *Phys. Rev. B* **101**, 205407 (2020).
170. Yang, M. et al. Creation of skyrmions in van der Waals ferromagnet Fe_3GeTe_2 on $(Co/Pd)_n$ superlattice. *Sci. Adv.* **6**, eabb5157 (2020).
171. Ding, B. et al. Observation of magnetic skyrmion bubbles in a van der Waals ferromagnet Fe_3GeTe_2. *Nano Lett.* **20**, 868–873 (2020).
172. Meijer, M. J. et al. Chiral spin spirals at the surface of the van der Waals ferromagnet Fe_3GeTe_2. *Nano Lett.* **20**, 8563–8568 (2020).
173. Liang, J. et al. Very large Dzyaloshinskii-Moriya interaction in two-dimensional Janus manganese dichalcogenides and its application to realize skyrmion states. *Phys. Rev. B* **101**, 184401 (2020).
174. Zhang, L. et al. Proximity-coupling-induced significant enhancement of coercive field and Curie temperature in 2D van der Waals heterostructures. *Adv. Mater.* **32**, 2002032 (2020).
175. Giustino, F. et al. The 2020 quantum materials roadmap. *J. Phys. Mater.* **3**, 042006 (2020).
176. Lin, X., Yang, W., Wang, K. L. & Zhao, W. Two-dimensional spintronics for low-power electronics. *Nat. Electron.* **2**, 274–283 (2019).
177. Savero Torres, W. et al. Magnetism, spin dynamics, and quantum transport in two-dimensional systems. *MRS Bull.* **45**, 357–365 (2020).
178. Kamalakar, M. V., Groenveld, C., Dankert, A. & Dash, S. P. Long distance spin communication in chemical vapour deposited graphene. *Nat. Commun.* **6**, 6766 (2015).
179. Ingla-Aynés, J., Kaverzin, A. A. & van Wees, B. J. Carrier drift control of spin currents in graphene-based spin-current demultiplexers. *Phys. Rev. Appl.* **10**, 044073 (2018).
180. Qi, J., Li, X., Niu, Q. & Feng, J. Giant and tunable valley degeneracy splitting in $MoTe_2$. *Phys. Rev. B* **92**, 121403 (2015).

Acknowledgements

We thank D. Torres (ICN2) for help in implementing the 3D device models used in the figures. J.F.S. and S.O.V. acknowledge support of the European Union's Horizon 2020 FET-PROACTIVE project TOCHA under grant agreement 824140, the King Abdullah University of Science and Technology (KAUST) through award number OSR-2018-CRG7-3717 and MINECO under contract numbers PID2019-111773RB-I00/AEI/10.13039/501100011033, RYC2019-028368-I/AEI/10.13039/50110001103 and SEV-2017-0706 Severo Ochoa. J.F., S.R. and S.O.V. acknowledge support from the European Union Horizon 2020 Research and Innovation Program under contract number 881603 (Graphene Flagship) and J.F. acknowledges support from the Deutsche Forschungsgemeinschaft (DFG, German research Foundation) under grant numbers SFB 1277 (project-id:314695032) and SPP 2244. R.K.K. acknowledges support from the US DOE-BES (grant number DE-SC0016379), AFOSR MURI 2D MAGIC (grant number FA9550-19-1-0390) and NSF MRSEC (grant number DMR-2011876).

Competing interests

The authors declare no competing interests.

Additional information

Correspondence should be addressed to J.F.S. or S.O.V.

Peer review information *Nature Nanotechnology* thanks Guo-Xing Miao, Stefano Sanvito and the other, anonymous, reviewer(s) for their contribution to the peer review of this work.